Petroleum Science 18 (2021) 1589–1610

Contents lists available at ScienceDirect

Petroleum Science

journal homepage: www.keaipublishing.com/en/journals/petroleum-science

Original Paper

How argillaceous reservoirs exhibit better quality than silty mudstones? Anomalous behavior of shale gas-bearing properties of continental fine-grained sediments in Southwest China and its possible forcing mechanisms

Wei Yang [a, b, *], Liang Xu [a, b], Dong-Xia Chen [a, c], Zhen-Xue Jiang [a, b], Zi-Ya Zhang [a, b, d, e], Bin Hao [f], Ru-Si Zuo [a, b], Qian-You Wang [a, b], Rong Chen [d, e]

[a] State Key Laboratory of Petroleum Resources and Prospecting, China University of Petroleum (Beijing), Beijing, 102249, China
[b] The Unconventional Oil and Gas Institute, China University of Petroleum (Beijing), Beijing, 102249, China
[c] College of Geosciences, China University of Petroleum, Beijing, 102249, China
[d] Oil & Gas Survey, China Geological Survey, Beijing, 100029, China
[e] The Key Laboratory of Unconventional Petroleum Geology, China Geological Survey, Beijing, 100029, China
[f] Northwest Branch, PetroChina Research Institute of Petroleum Exploration and Development, Lanzhou, Gansu 730020, China

ARTICLE INFO

Article history:
Received 28 November 2020
Accepted 2 March 2021
Available online 21 September 2021

Edited by Jie Hao and Teng Zhu

Keywords:
Granularity
Silty-mud sediments
Reservoir quality
Bitumen pores
Clay mineral
Differential reservoir-forming

ABSTRACT

Achieving a thorough understanding of how primary sedimentary granularity drives considerable heterogeneity in internal reservoir attributes of terrigenous fine-grained deposits is of great significance. We investigated the quantitative differentiation and its corresponding driving forces of physical reservoir properties and pore-structure characteristics of silty-mud sediments in the Upper Triassic Xujiahe Formation (SW China) using a multi-method approach. The results show that the micro-mesopore volume and surface area of mudstones/shales are apparently higher than those of silty mudstones and a remarkable threefold rise in average permeability also presents. Extensively distributed bitumen pores occurring mostly along brittle mineral grains or forming clay-organic complexes make considerable contributions to shrinking microcracks. Furthermore, an evidently higher concentration of clay minerals in mudstone/shale reservoirs is primarily responsible for development of the two types of clay intercrystalline pores distributed along grain aggregates and between well-oriented platelets. These two major causes facilitate the formation of micro-bedding fractures/non-bedding microfractures and connected fracture and pore-fracture networks, and also high-quality argillaceous reservoirs by strongly enhancing storage spaces and seepage capacities. Finally, a conceptual model is established for interpreting a differential reservoir-forming mechanism and corresponding two-sided effects on petrophysical and reservoir quality properties for continental silty-mud sediments.

1. Introduction

Fine-grained sedimentary rocks consisting of silty-mud sediments with grain sizes of less than 62 μm and at concentrations of 50% are largely defined as the most important reservoirs and exploration targets for unconventional hydrocarbon resources (Spears et al., 1980; Zhou et al., 2016; Jiang et al., 2017). Continental fine-grained cyclothemic sequences composed of organic-rich mudstones/shales and relatively organic-poor silty mudstones/siltstones are characterized by rapidly changing thicknesses, forming classical and basic source-reservoir assemblage types with great hydrocarbon significance (Li et al. 2015, 2016;; DeReuil and Birgenheier, 2019). Unconventional oil and gas resources accumulating in continental tight reservoirs in close contact with ideal source rock intervals are thought to be realistic and even favorable targets of exploration and development (Wang et al., 2011; Yao et al., 2013).

* Corresponding author. State Key Laboratory of Petroleum Resources and Prospecting, China University of Petroleum (Beijing), Beijing, 102249, China.
E-mail address: yangw@pku.edu.cn (W. Yang).

https://doi.org/10.1016/j.petsci.2021.09.032

In general, the granularity dependence of petrophysical properties of terrigenous clastic sediments is remarkable as manifested by gradual reductions in laboratory-measured porosity and permeability as reservoirs tend to be finer grained and progressively densified. Previous investigations have focused on grain size as a sole factor influencing the theoretical porosity-permeability properties of fine-grained deposits and preliminary quantitative estimations have been carried out, which is indicative of a non-ignorable effect of initial equivalent granularity (Worden et al., 1997; Wang, 2007; Jin et al., 2016; Zeng et al., 2016). A stepwise increasing trend in primary microscopic pore size and pore connectivity is also discernible (in the following order: mudstones, silty mudstones and argillaceous siltstones) from continental fine-grained sediments (Xu et al., 2013; Olivarius et al., 2015; Liu et al., 2018).

However, it is worth noting that uncommon and even anomalous characteristics of micropore parameters have been recorded in certain fine-grained lacustrine depositional systems, as reflected by the significantly lower average mesopore volumes found in silty laminated shales than in massive shales (Liu et al., 2019b). In view of rare documentation and thus poor understanding of the potential preponderance of reservoir properties in continental mudstones, more reliable constraints on the differentiation of porosity/permeability and pore-structure features are urgently needed and likely to be of great interest to earth scientists and petroleum geologists, focused on fluvio-lacustrine lithological associations formed by alternating or sandwich-like mudstones and silty mudstones undergoing an equivalent diagenesis regime (Milliken, 2014; Yang et al., 2019a, b).

Continental fine-grained sedimentary facies of the Upper Triassic Xujiahe Formation, which are widely distributed across the western subsiding Sichuan Basin (SW China), are targeted as a key hydrocarbon exploration series demonstrating strong tight and shale gas resource potential (Zou et al. 2010, 2019;; Zhang et al., 2012; Li et al., 2014). The characteristic interbedding of silt and mud sediments in shale-dominated Xu3 (T_3x^3) and Xu5 (T_3x^5) members offers particularly useful settings and valuable archives for accurately describing reservoir micro-heterogeneity associated with particle size differences (Zhu et al., 2009; Zhao et al., 2010; Huang et al., 2015; Xu et al., 2015; Chen et al., 2016a; Dai et al., 2016). More importantly, excellent petrophysical properties have been identified in mudstones/shales, highlighting the need to perform systematic investigations of forcing mechanisms of the potential anomalous behaviors of reservoir capacity.

In focusing on newly cored samples collected from the Xu3 (T_3x^3) and Xu5 (T_3x^5) members of the Upper Triassic Xujiahe Formation in the western subsiding Sichuan Basin, this study carried out comprehensive and detailed sediment granularity analysis, total organic carbon (TOC) measurements and rock pyrolysis testing, field emission scanning electron microscopy (FE-SEM) observations, X-ray diffraction (XRD) experiments (whole-rock and clay minerals), low-pressure N_2 and CO_2 adsorption analysis, high-pressure mercury intrusion (HPMI), and physical property measurements. The aim of this study is to thoroughly investigate possible causes and driving mechanisms of granularity-induced anomalies in reservoir quality as identified from fine-grain-depositing series. This investigation also sought to produce a relevant and interpretive model illustrating the differential reservoir-forming patterns of fluvio-lacustrine silty-mud sediments to guide the effective prediction of internal reservoir heterogeneities and to provide theoretical support for the future exploration and assessment of unconventional natural gas resources in similar terrestrial basins.

2. Geological setting and stratigraphy

The Sichuan Basin, located in the southwestern China, is one of the most gas-productive superimposed basins developing on the western part of the Yangtze Craton, with an area of more than 1.8×10^5 km^2 (He et al., 2011a; Zhu et al., 2015; Jin et al., 2018) (Fig. 1a). It is bounded by series of mountains forming the landform nowadays due to several orogenic events, especially the India-Asian collision (Wang et al., 1989; Liang et al., 2014; Yang et al. 2018, 2019b). More than 10 km-thick sediments were deposited in the Sichuan Basin throughout the Late Neoproterozoic to Mesozoic times, and a series of black shale sequences were developed during the Ediacaran, Early Cambrian, Late Ordovian-Early Silurian, Permian, and Late Triassic-Early Jurassic periods (Zou et al. 2010, 2014; Liu et al., 2018). Continental shale gas has been mainly produced from the Mesozoic series (Huang et al., 2015).

The continental Upper Triassic Xujiahe Formation, which is widely distributed across the western Sichuan Basin, acts as a key hydrocarbon exploration series with a considerable shale gas resource potential. The targeted Ledi 1 Well located in the Jiajiang area on the southern margins of the western subsiding Sichuan Basin (Fig. 1a) was recently drilled for continental shale gas exploration in the Xujiahe Formation, which can be subdivided into six members in ascending order. The Xu1 (T_3x^1), Xu3 (T_3x^3), and Xu5 (T_3x^5) members are mainly composed of dark grey to grey mudstones, shales, and silty mudstones interbedded with coal seams deposited in braided river delta plains, braided river delta fronts, and lacustrine-swamp environments, creating conditions suitable for the preservation of humic organic matter (Dai et al., 2016; Jiang et al., 2017) (Fig. 1b and Tables 1 and 2). The Xu2 (T_3x^2), Xu4 (T_3x^4), and Xu6 (T_3x^6) members are mainly characterized by medium-to-coarse-grained feldspar-quartz and pebbly feldspar sandstones interbedded with a small amount of siltstone and grey shale and coal seams locally developed in braided river delta plains and front sub-facies. The Xu1 (T_3x^1), Xu3 (T_3x^3), and Xu5 (T_3x^5) members include basic conditions for the generation of continental shale gas while the Xu2, Xu4, and Xu6 members act as reservoir rocks for several tight gas fields (including the Xinchang gas field) in the western Sichuan Basin (Dai et al., 2014; Huang et al., 2015; Liu et al., 2019c).

The targeted Ledi 1 Well, located at the Jiajiang area of the southern margin of the western Sichuan subsiding Basin (Fig. 1a), was recently drilled to target for continental shale gas exploration focusing on the Upper Triassic Xujiahe Formation. The shale-dominated Xu3 (T_3x^3) and Xu5 (T_3x^5) members mainly consist of grey and black medium to thick-bedded carbonaceous mudstones and shales, mostly interbedded with thin-bedded argillaceous siltstones and fine-grained sandstones (Fig. 1b), with a set of coal layers extensively distributed. On the contrary, the sandstone-dominated Xu2, Xu4 and Xu6 members are commonly characterized by intercalations of grey medium to thick-bedded medium- and fine-grained sandstones, argillaceous siltstones, and black thin-bedded carbonaceous mudstones and shales. The shale-dominated members were interpreted to be predominantly composed of mudflat, coal-bearing swamp, and interdistributary bay microfacies deposited in shore-shallow lacustrine and delta-front environments, respectively.

3. Samples and analytical methods

3.1. Samples

Based on refined core observations and descriptions of the investigated Ledi 1 Well, a total of 45 representative core samples from the targeted Xu3 (T_3x^3) and Xu5 (T_3x^5) continental mudstone/

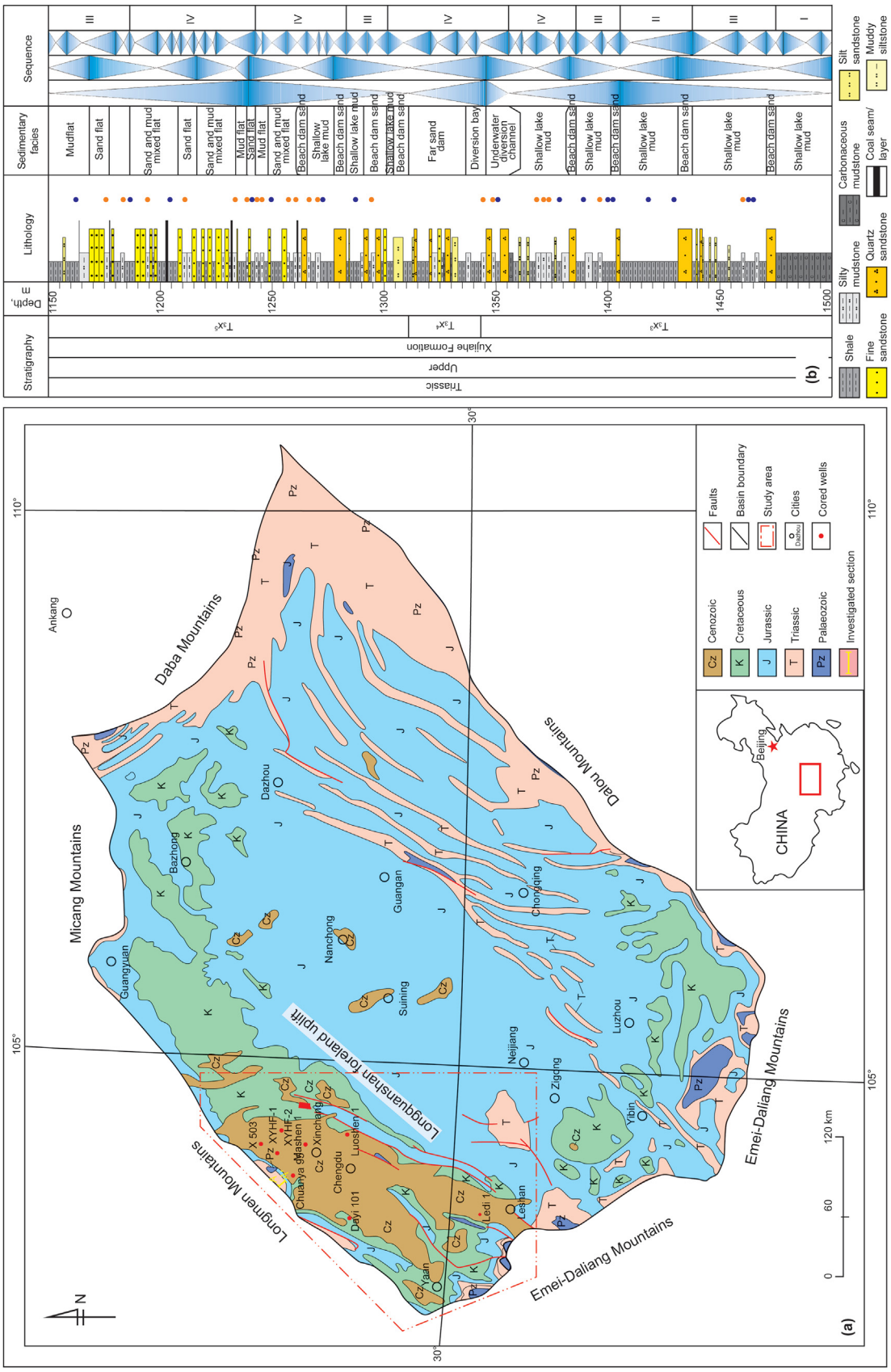

Fig. 1. (a) Tectonic and geological setting of the Sichuan Basin with the approximate location of the western Sichuan Depression shown with a dashed box (modified from Yang et al., 2019). The investigated cored Well Ledi 1 and other involved well sites are displayed in detail in the western Sichuan subsiding Basin (modified from Yang et al., 2019b). (b) A comprehensive lithological column of the Xu3 (T_3x^3), Xu4 (T_3x^4) and Xu5 (T_3x^5) members in the Upper Triassic Xujiahe Formation of the cored Well Ledi 1. Blue and orange dots indicate sampling locations of mudstones/shales and silty mudstones, respectively.

Table 1
Bulk and clay mineralogical composition of the argillaceous and silty mudstone samples from the Xu3 (T_3x^3) and Xu5 (T_3x^5) members of the Upper Triassic Xujiahe Formation.

Sample ID	Depth, m	Lithology		Quartz	Potassium feldspar	Plagiocl-ase	Calcite	Dolomite	Pyrite	Clay mineral	Sample ID	Depth, m	Kaolinite	Chlorite	Illite	I/S	C/S
LD-2	1163.38	Mudstones/shales	AL	45.6	0.7	1.2	0	1.7	0	50.8	LD-25	1186.40	85.0	/	5.0	10.0	/
LD-7	1168.38		AL	37.6	0.6	1.0	0	2.7	0	58.1							
LD-13	1174.38		AL	40.3	0.7	1.2	0	5.7	0	52.1							
LD-25	1186.40		AL	43.8	0.9	1.9	0	0	0	53.4	LD-30	1191.40	7.0	10.0	19.0	58.0	6.0
LD-29	1190.40		AL	32.2	0.7	1.9	0	8.1	0	57.1							
LD-31	1192.40		AL	25.5	0.9	2.5	0	0	0	71.1							
LD-38	1199.40		AL	27.5	1.0	1.9	6.9	6.9	0	55.8	LD-55	1216.40	8.0	3.0	8.0	80.0	1.0
LD-61	1222.40		AL	26.2	0.8	3.0	6.2	9.0	0	54.8							
LD-80	1241.40		AL	29.9	0.9	2.9	0	7.8	0	58.5							
LD-90	1251.40		AL	33.0	0.9	3.0	0	0	0	63.1	LD-59	1220.40	18.0	7.0	11.0	61.0	3.0
LD-111	1272.30		AL	28.5	0.7	3.3	2.6	4.2	0	60.7							
LD-118	1279.30		AL	26.8	1.0	3.2	3.4	6	0	59.6							
LD-129	1290.30		AL	20.4	0.9	1.9	0	8.4	0.5	67.9	LD-78	1239.40	10.0	7.0	12.0	66.0	5.0
LD-151	1350.50		AL	41.3	0.4	5.1	0	8.7	0	44.5							
LD-156	1378.10		AL	35.3	0.8	3.6	0	7.4	0	52.9							
LD-167	1389.10		AL	35.7	0.7	4.9	0	5.1	0	53.6	LD-146	1345.50	3.0	5.0	13.0	74.0	5.0
LD-170	1392.10		AL	29.1	1.0	5.6	0	13.1	0	51.2							
LD-177	1400.10		AL	40.7	0.7	6.1	0	11.6	0	40.9							
LD-191	1418.10		AL	37.4	1.0	5.0	0	10.3	0	46.3	LD-210	1373.10	6.0	6.0	9.0	76.0	3.0
LD-197	1353.00		AL	39.0	0.7	4.8	0	0	0	55.5							
LD-200	1359.00		AL	33.9	0.8	5.8	0	0	0	59.5							
LD-215	1429.70		AL	31.9	0.8	3.9	0	10	0	53.4							
LD-216	1431.70		AL	25.2	0.9	3.4	0	7.7	0	62.8	LD-166	1388.10	3.0	5.0	10.0	79.0	3.0
LD-217	1433.70		AL	36.5	0.9	4.2	0	3.3	0	55.1							
LD-231	1456.70		AL	29.0	0.9	4.4	6.3	0	0	59.4							
Distribution range				20.4–45.6	0.4–1.0	1.0–6.1	0.0–6.9	0.0–13.1	0.0–0.5	40.9–71.1	LD-169	1391.10	3.0	6.0	13.0	76.0	2.0
Average value				33.3	0.8	3.4	1.0	5.5	0.0	55.9							
LD-22	1183.40	Silty mudstones	AL	33.2	0.6	2.3	4.3	7.1	0	52.5							
LD-50	1211.40		AL	38.7	0.9	2.5	3.1	5.8	0	49.0							
LD-78	1239.40		SL	47.7	0.7	7.1	0	6	0	38.5	LD-180	1403.10	4.0	7.0	10.0	75.0	4.0
LD-82	1243.40		SL	49.4	0.5	6.5	1.8	5.5	0	36.3							
LD-85	1246.40		SL	60.5	0.4	4.9	7.9	8.8	0	17.5							
LD-96	1257.40		SL	47.2	0.4	8.1	3.8	5.7	0	34.8							
LD-105	1266.40		SL	43.7	0.4	6.5	2.8	7.6	0	39	LD-178	1401.10	3.0	6.0	10.0	77.0	4.0
LD-133	1294.30		AL	36.6	0.5	5.6	1.5	12.7	0.3	42.8							
LD-149	1348.50		SL	56.5	0.4	5.5	0	10.5	0	27.1							
LD-162	1384.10		AL	32.4	0.7	5.6	0	10.2	0	51.1							
LD-173	1396.10		AL	31.9	0.6	4.9	1.7	10.7	0	50.2	LD-194	1423.10	7.0	9.0	13.0	65.0	6.0
LD-201	1360.00		AL	36.6	0.5	8.2	0	10.6	0	44.1							
LD-206	1368.10		AL	33.2	0.7	4.2	0	12.1	0	49.8							
LD-210	1373.10		AL	34.2	0.8	5.4	0	10.8	0	48.8							
LD-224	1445.70		AL	30.1	0.7	4.7	0	7.7	0	56.8	LD-228	1451.70	2.0	5.0	11.0	79.0	3.0
LD-235	1462.70		AL	40.6	0.7	5.0	7.9	0	0	45.8							
Distribution range				30.1–60.5	0.4–0.9	2.3–8.2	0.0–7.9	0.0–12.7	0.0–0.3	17.5–56.8							
Average value				40.8	0.6	5.4	2.2	8.2	0.0	42.8							
Total distribution range				20.4–60.5	0.4–1.0	1.0–8.2	0.0–7.9	0.0–13.1	0.0–0.5	17.5–71.1	–		2.0–18.0	3.0–10.0	8.0–19.0	58.0–80.0	1.0–6.0
Total average value				36.2	0.7	4.2	1.5	6.6	0.0	50.8	–		6.2	6.3	11.6	72.2	3.8

Table 2
The fraction component percentages for grain-size distribution pattern of the argillaceous and silty mudstone reservoirs of the Xu3 (T_3x^3) and Xu5 (T_3x^5) members in the Upper Triassic Xujiahe Formation.

Lithology	Sample	Depth, m	$\Phi \geq 8$	$4 \leq \Phi < 8$	$\Phi < 4$
Mudstones/shales	LD-7	1168.38	50.29%	49.71%	0
Mudstones/shales	LD-25	1186.40	48.13%	51.87%	0
Mudstones/shales	LD-29	1190.40	43.07%	56.93%	0
Mudstones/shales	LD-38	1199.40	58.64%	41.36%	0
Mudstones/shales	LD-90	1251.40	57.60%	42.40%	0
Mudstones/shales	LD-111	1272.30	55.00%	45.00%	0
Mudstones/shales	LD-129	1290.30	76.12%	23.88%	0
Average			55.55%	44.45%	0
Silty mudstones	LD-50	1211.40	46.59%	53.41%	0
Silty mudstones	LD-78	1239.40	44.68%	55.32%	0
Silty mudstones	LD-96	1257.40	29.03%	61.28%	9.69%
Silty mudstones	LD-105	1266.40	31.01%	63.87%	5.12%
Silty mudstones	LD-133	1294.30	37.29%	62.67%	0.04%
Silty mudstones	LD-224	1445.70	38.32%	61.65%	0.03%
Silty mudstones	LD-235	1462.70	41.08%	58.92%	0
Average			38.29%	59.59%	2.13%

shale and silty mudstone reservoirs were measured and analyzed at sampling intervals of approximately from 2 to 5 m.

3.2. Sediment grain-size analysis

Grain-size analysis is an invaluable tool for investigating the origins of terrigenous sediments and deposited settings, which can be identified from corresponding individual characteristic granularity distribution patterns (Zheng et al., 2003; Yu et al., 2014; Fenster et al., 2016; Ge et al., 2018; Clift et al., 2019; Wu et al., 2019). Sample preparation and analysis followed standard procedures (Lu and An, 1997; Wang et al., 2016). Representative powder samples of 0.5–0.8 g were dissolved in 10 mL of 30% hydrogen peroxide (H_2O_2) to remove organic matter, and then all authigenic carbonate and pedogenic clay minerals were removed using 10–20 mL of 10% HCl to ensure that the granularity of original particles could be analyzed. Subsequently, 10 mL of 0.05 N (equivalent concentration) sodium hexametaphosphate [$(NaPO_3)_6$] was added to disperse the particles, and the beaker used was vibrated ultrasonically for roughly 10 min (Zheng et al., 2003; Wu et al., 2019). Finally, grain-size measurements of the prepared samples were carried out using the Malvern Mastersizer 3000 laser grain-size analysis system housed at the State Key Laboratory of Petroleum Resources and Prospecting, China University of Petroleum (Beijing). The particle size range for measurements was set as 0.01–3500 μm.

3.3. TOC and rock pyrolysis

TOC analysis was performed to measure the organic matter content of the shale samples using a Leco CS-230 carbon analyser. In this study, rocks with TOC values exceeding 0.5–1.0 wt% are inferred to be potential source rocks (Tissot and Welte, 1984). Rock-Eval pyrolysis analyses were performed using an OGE-II rock pyrolyser to characterize the type and thermal maturity of organic matter in the rocks.

3.4. FE-SEM analyses

Selected samples are observed via FE-SEM (FEI HELIOS NANOLAB 650 SEM) in combination with an energy dispersive X-ray spectrometer to analyse the continental shale pore structure at the micro- and nano-scales. A detailed description of the technical procedure is given in the Chinese Oil and Gas Industry Standards (SY/T5162-1997).

3.5. X-ray diffraction analysis

The bulk mineralogy of the shale samples was derived through the X-ray diffraction analysis of powder of less than 200 mesh (i.e., <75 mm) at Bangda New Technology Co., Ltd., Renqiu, China. The measurements were conducted using a Bruker D8 DISCOVER diffractometer (Co Kα-radiation, 45 kV, 35 mA) following the two independent processes of the CPSC procedure. Using a scintillation detector with a counting time of 20 s, the diffracted beam was measured for each step of 0.02° 2θ. Diffractograms were obtained from 2° to 76° 2θ.

3.6. Low-pressure N_2 and CO_2 adsorption analysis

An N_2 adsorption analysis of pore structures, including pore surface areas and pore volumes, was conducted using a Micromeritics® Tristar II 3020 analyser. The pore surface areas of the shale samples were analyzed using the multilayer Brunauer Emmett Teller (BET) theory (Gregg and Sing, 1982; Mendhe et al., 2017), and pore volumes were analyzed following the Barrett-Joyner-Halenda (BJH) method (Scherdel et al., 2010). N_2 adsorption analysis was primarily used to study mesopore structures.

The micropore structure of the shale samples was characterized using the CO_2 gas isothermal adsorption method at 273.15 K (cold water bath). The distribution of micropores size can be calculated from the Density-Functional-Theory (DFT) model because CO_2 gas can enter a pore with a diameter of 0.35 nm. CO_2 adsorption analysis was performed using an Autosorb-IQ-MP manufactured by Quantachrome, USA.

3.7. High-pressure mercury intrusion porosimetry (HPMI)

As essential and effective techniques widely used to quantitatively characterize the pore-throat size distribution in porous materials (Chalmers et al., 2012; Gao et al., 2018), HPMI measurement was performed at the Key Laboratory of Tectonics and Petroleum Resources Ministry of Education, China University of Geosciences (Wuhan) using a mercury intrusion porosimeter (Autopore IV 9520) in accordance with Chinese national standard GBT21650.1-2008. A single cuboid was placed into a penetrometer with a 0.096 mL stem volume during the HPMI test, which is suitable for low-porosity (less than 8%) fine-grained sediment samples. Mercury compressibility at high pressure levels was corrected (Sun et al., 2019; Wang et al., 2019).

3.8. Petrophysical analysis

Sixty-one continental shale samples were collected from the Upper Triassic Xujiahe Formation to examine their petrophysical characteristics. The KXD-III helium porosity determinator manufactured by the Unconventional Oil and Gas Institute in the China University of Petroleum (Beijing) was used for helium-based porosity measurements. The ULTRA-PERM^{TM}200 permeability tester manufactured by Bangda New Technology Co., Ltd., Renqiu, China was used for pulse decay permeability measurements using nitrogen and recording data every 30 s following Chinese Oil and Gas Industry Standards (SY/T5336-1996).

4. Results

4.1. Classification of lithofacies of continental fine-grained sediments

According to our X-ray diffraction analysis, the continental fine-grained sediment samples are mostly composed of clay minerals with subordinate quartz, dolomite, plagioclase, calcite, minor potassium feldspar and pyrite (Fig. 2a and b). Specifically, total concentrations of clay minerals in the mudstone/shale facies were considerably greater than those of the silty mudstone category, ranging from 40.9% to 71.1% with an average of 55.9% and ranging from 17.5% to 56.8% with an average of 42.8%, respectively (Fig. 2a and b; Table 1). Mixed-layer illite-smectite are generally the most prominent component found in the composition of clay minerals contained in the argillaceous facies, and illite is the second most abundant species (Fig. 2c).

According to the three-end diagram of concentrations of siliceous minerals (quartz and feldspar), carbonate minerals, and clay minerals, a total of four lithofacies groups for Xujiahe continental shales in the study area are classified (Fig. 2d) as siliceous shale lithofacies (SL), argillaceous shale lithofacies (AL), calcareous shale lithofacies (CL), and argillaceous/siliceous mixed shale lithofacies (ASML) (Fig. 2d). Specifically, when the siliceous mineral concentration is more than 75%, the shale lithofacies falls into the category of siliceous shale lithofacies group; when the carbonate mineral content is higher than 60%, it falls into the category of calcareous shale lithofacies group; when the clay mineral concentration is greater than 40%, it falls into the category of argillaceous shale lithofacies group; when the clay mineral content is lower than 40%, and the concentrations of carbonates and siliceous-end members span from 25% to 75%, it falls into the category of mixed shale lithofacies group. In combination with lithological characteristics of continental fine-grained sedimentary series of the Upper Triassic Xujiahe Formation (Bian et al., 2009; Huang et al., 2016), all visualized data for our study pertain to argillaceous and siliceous shale lithofacies. More specifically, mudstones/shales are dominant and silty mudstones are a minority within the AL zone while the SL zone is only constituted by silty mudstone samples (Fig. 2d).

4.2. Grain-size distributions of the silty-mud sediment samples

As shown in Fig. 3, grain-size distributions of the mudstone/shale facies are generally characterized by unimodal behavior with two sub-peaks at 3 μm and 4 μm, respectively (Fig. 3c). In comparison, grain-size distribution curves of the silty mudstones from the investigated continental fine-grained sedimentary sequence of the Upper Triassic Xujiahe Formation show two sub-peaks at 8 μm and 10 μm, though a unimodal pattern is also present (Fig. 3d).

The demonstrated difference in granularity distribution characteristics of the mudstones/shales and silty mudstones is also remarkable from the probability cumulative curves (Fig. 3a and b). According to the particle-size conversion formula ($\Phi = \neg \log_2 D$ (Grain Size)) (Zhu et al., 2008; Yu et al., 2014) and the traditional boundary Φ value at 8 between argillaceous ($\Phi > 8$) and silty mudstones ($\Phi < 8$) (Table 2), the fraction component percentage for the grain diameter (Φ) range of 8–13 for mudstones/shales is strikingly higher than that for silty mudstones. Correspondingly, components with a grain diameter (Φ) of less than 7 account for a significantly larger proportion in silty mudstones than in the argillaceous facies (Fig. 3a and b). The observed grain-size distribution patterns thus correspond well with the classification of the two defined

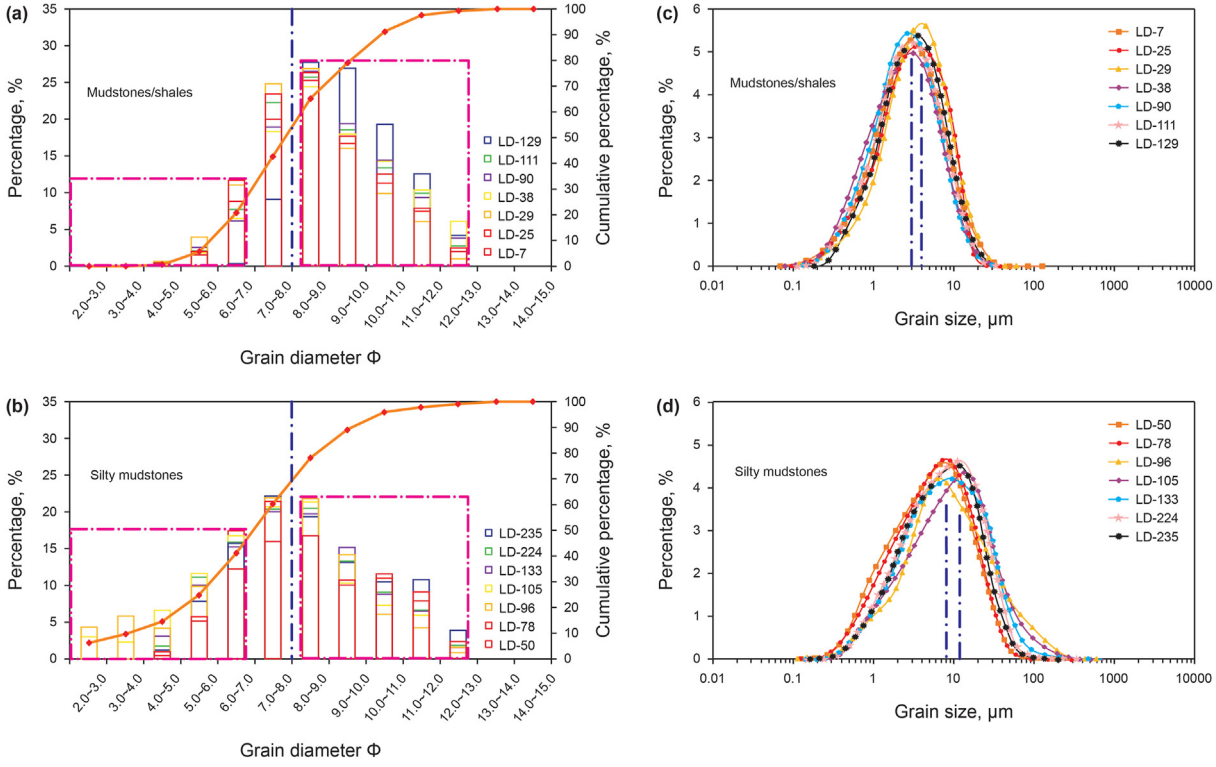

Fig. 2. (a, b) whole-rock mineral composition bar charts of the continental mudstones/shales and silty mudstones of the Xu3 (T_3x^3) and Xu5 (T_3x^5) members of the Upper Triassic Xujiahe Formation. It is noticeable that there is a relatively major difference in the total clay concentration. (c) Clay mineral composition bar chart of the argillaceous reservoirs of the Xu3 (T_3x^3) and Xu5 (T_3x^5) members of the Upper Triassic Xujiahe Formation. (d) Ternary diagram of the mineralogy of the argillaceous and silty mudstone reservoirs in the Upper Triassic Xujiahe Formation.

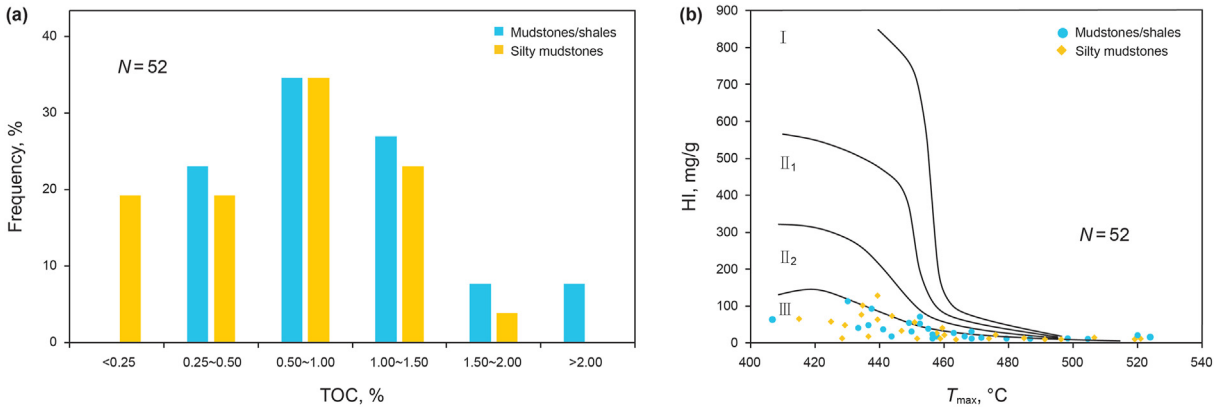

Fig. 3. (a, b) Statistical histograms and cumulative probability distributions of sediment grain-size parameters obtained respectively from representative argillaceous and silty mudstone samples from the Xu3 (T_3x^3) and Xu5 (T_3x^5) members of the Upper Triassic Xujiahe Formation. (c, d) Sediment grain-size distributions of representative argillaceous and silty mudstone samples, respectively, from silty-mud units of the Upper Triassic Xujiahe Formation.

lithofacies in the investigated silty-mud sediments (Fig. 3).

4.3. TOC abundance and types of organic matter

TOC concentrations in samples drawn from continental silty-mud sediments in the shale-dominated Xu3 (T_3x^3) and Xu5 (T_3x^5) members range widely from 0.10% to 3.46% (average 0.92%). TOC abundance from the argillaceous facies (ranging between 0.36% and 3.46%, and averaging 1.12%) is considerably higher than that from the silty mudstones (ranging between 0.10% and 1.94%, and averaging 0.72%) (Fig. 4a; Table 3). The kerogen in our targeted fine-grained sediments is mainly composed of organic matter of Type III with Type II_2 representing a minority as revealed by our cross plot of T_{max} values versus the hydrogen index (HI) (Fig. 4b; Table 3) and as previously identified from maceral compositions (Yang et al., 2019b), suggesting that terrigenous organic matter mainly consists of humic types, exhibiting enriched concentrations of non-hydrocarbon compounds (resins) and asphaltenes (Jin, 2010; Chen and Xiao, 2014).

4.4. Microscopic pore types in continental argillaceous and silty mudstone reservoirs

From our FE-SEM observations and the shale reservoir space type classifications of previous studies, the following major pore types in the Upper Triassic Xujiahe Formation are identified:

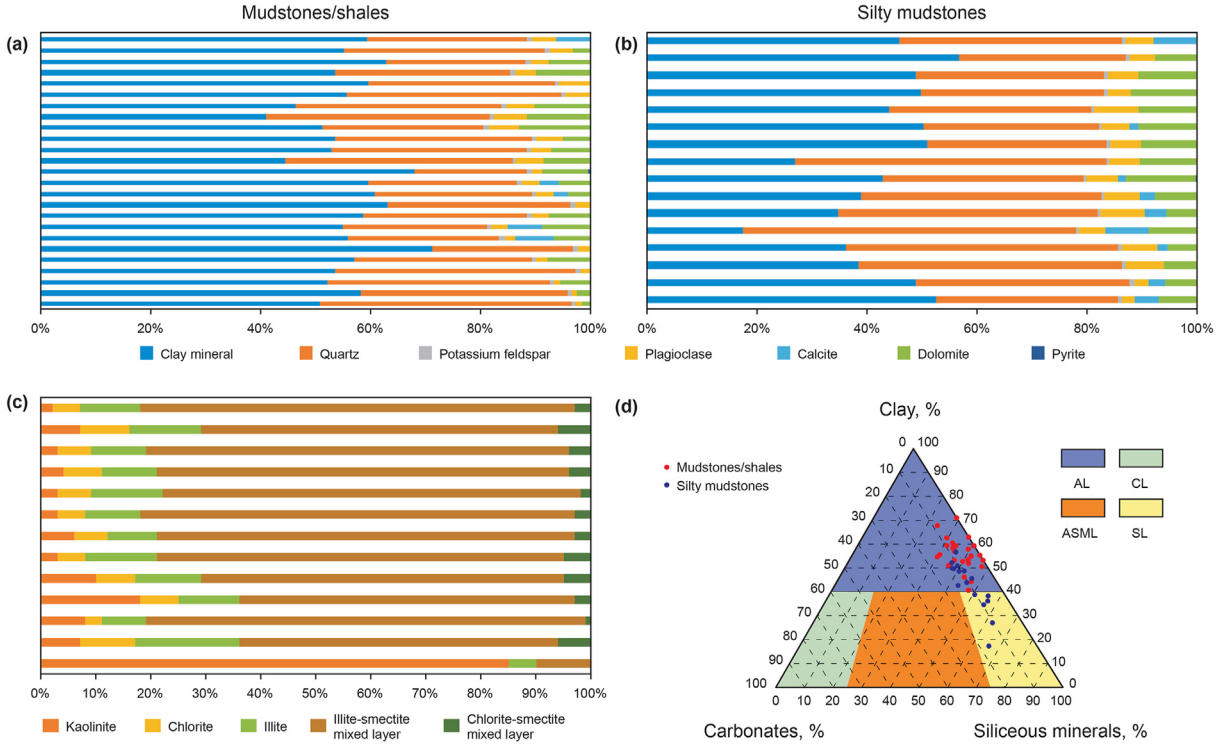

Fig. 4. (a) The TOC distribution characteristics of the continental mudstone/shale and silty mudstone reservoirs from the Xu3 (T_3x^3) and Xu5 (T_3x^5) members of the Upper Triassic Xujiahe Formation. (b) HI-T_{max} graphic showing kerogen types of continental mudstones/shales and silty mudstones from the Xu3 (T_3x^3) and Xu5 (T_3x^5) members of the Upper Triassic Xujiahe Formation (modified Van Krevelen diagram) (Espitalie et al., 1977).

Table 3
The TOC histogram and HI-T_{max} graphic showing the organic matter abundance and kerogen types of the Xu3 (T_3x^3) and Xu5 (T_3x^5) members in the Upper Triassic Xujiahe Formation.

Sample	Lithology	Depth, m	TOC, %	T_{max}, °C	HI, mg/g	Kerogen Type
LD-1	Mudstones/shales	1162.40	0.816	407	62.626	III
LD-2	Mudstones/shales	1163.38	0.420	430	112.777	III
LD-7	Mudstones/shales	1168.38	0.476	433	40.312	III
LD-13	Mudstones/shales	1174.38	1.356	437	47.603	III
LD-25	Mudstones/shales	1186.40	1.370	438	92.933	III
LD-29	Mudstones/shales	1190.40	0.826	441	36.786	III
LD-31	Mudstones/shales	1192.40	1.899	444	17.786	III
LD-38	Mudstones/shales	1199.40	0.908	450	31.463	III
LD-61	Mudstones/shales	1222.40	0.758	449	55.017	III
LD-80	Mudstones/shales	1241.40	0.706	453	71.375	II_2
LD-90	Mudstones/shales	1251.40	0.371	453	52.342	II_2
LD-111	Mudstones/shales	1272.30	0.470	455	38.780	III
LD-118	Mudstones/shales	1279.30	1.310	456	11.607	III
LD-129	Mudstones/shales	1290.30	3.460	456	24.296	III
LD-151	Mudstones/shales	1350.50	1.311	458	17.062	III
LD-156	Mudstones/shales	1378.10	0.895	463	27.100	III
LD-167	Mudstones/shales	1389.10	1.629	466	18.080	III
LD-170	Mudstones/shales	1392.10	1.452	468	30.796	II_2
LD-177	Mudstones/shales	1400.10	0.872	468	11.763	III
LD-191	Mudstones/shales	1418.10	0.824	472	14.522	III
LD-197	Mudstones/shales	1353.00	0.489	479	12.810	III
LD-200	Mudstones/shales	1359.00	2.455	487	11.093	III
LD-215	Mudstones/shales	1429.70	1.422	498	13.055	III
LD-216	Mudstones/shales	1431.70	0.810	505	11.323	III
LD-217	Mudstones/shales	1433.70	0.363	520	22.401	III
LD-231	Mudstones/shales	1456.70	1.344	524	17.013	III
LD-3	Silty mudstones	1164.38	0.168	415	65.060	III
LD-4	Silty mudstones	1165.38	0.097	425	57.831	III
LD-14	Silty mudstones	1175.40	1.279	428	12.651	III
LD-22	Silty mudstones	1183.40	0.811	429	48.795	III
LD-33	Silty mudstones	1194.40	0.306	434	76.807	III
LD-50	Silty mudstones	1211.40	0.288	435	102.108	III
LD-72	Silty mudstones	1233.40	1.944	439	63.253	III
LD-78	Silty mudstones	1239.40	0.900	439	129.217	II_2
LD-82	Silty mudstones	1243.40	0.260	437	17.169	III
LD-85	Silty mudstones	1246.40	0.156	444	73.193	III
LD-96	Silty mudstones	1257.40	1.177	447	32.530	III
LD-99	Silty mudstones	1260.40	0.244	451	56.024	II_2
LD-105	Silty mudstones	1266.40	0.204	452	11.747	III
LD-109	Silty mudstones	1270.30	0.337	459	11.747	III
LD-133	Silty mudstones	1294.30	0.989	458	27.108	III
LD-145	Silty mudstones	1344.50	0.922	460	21.687	III
LD-149	Silty mudstones	1348.50	0.583	460	40.663	II_2
LD-162	Silty mudstones	1384.10	0.900	464	9.036	III
LD-173	Silty mudstones	1396.10	0.914	474	12.651	III
LD-201	Silty mudstones	1360.00	0.766	476	22.590	II_2
LD-206	Silty mudstones	1368.10	1.124	485	13.554	III
LD-209	Silty mudstones	1372.10	0.466	491	9.940	III
LD-210	Silty mudstones	1373.10	1.016	496	10.843	III
LD-224	Silty mudstones	1445.70	1.120	507	13.554	III
LD-234	Silty mudstones	1460.70	0.639	519	9.940	III
LD-235	Silty mudstones	1462.70	1.092	521	11.747	III

organic matter pores, intragranular dissolved pores, and clay mineral intercrystalline pores (Fig. 5).

4.4.1. Residual primary pores

While most primary pores have been destroyed with the intensification of compaction and diagenesis in Upper Triassic Xujiahe continental shales, our observations show that a small number of intergranular unfilled initial pores still exist in situ, and the retained residual primary pores are supported by brittle mineral grains of materials such as quartz and feldspar (Fig. 5b).

4.4.2. Dissolved pores

Secondary intra- and intergranular dissolved pores with a wide range of pore diameters are well developed in soluble minerals such as calcareous matter and feldspar in the Upper Triassic Xujiahe Formation. Dissolved pores observed are generally poorly connected and isolated from each other (Fig. 5d), which is not favorable for shale gas accumulation, diffusion, and exploration.

4.4.3. Intercrystalline pores

Certain amounts of intercrystalline pores are found in clay minerals and framboidal pyrite crystal grains observed in Upper Triassic Xujiahe continental shales with pore diameters of approximately 10–500 nm. Clay mineral intercrystalline flake pores have formed through the dehydration of chlorite and illite whereas pyrite intercrystalline pores have developed due to the shedding of framboidal particles under local tectonic stress (Fig. 5b).

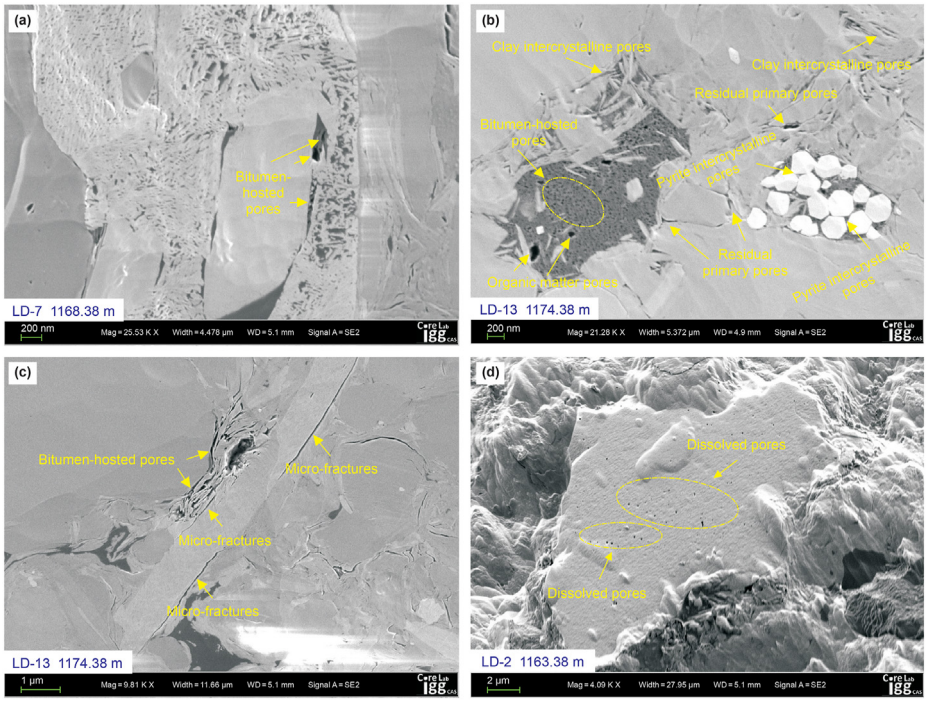

Fig. 5. Representative FE-SEM images of the continental silty-mud reservoir units of the Xu3 (T_3x^3) and Xu5 (T_3x^5) members exhibiting multi-type pore characteristics. (a) Bitumen-hosted pores; (b) Residual primary pores, bitumen-hosted and organic matter pores, and clay and pyrite intercrystalline pores; (c) Micro-fractures formed as the result of development of the bitumen-hosted pores; (d) Poorly connected and even isolated dissolved pores.

4.4.4. Organic matter pores

Compared to those of typical marine shales found in reservoirs (e.g., Devonian-Mississippian North America shales and Lower Silurian Longmaxi shales of SW China, organic matter pores in continental shale reservoirs appear to be less developed (Mastalerz et al., 2013; Guan et al., 2016; Liu et al., 2019a). However, secondary and bitumen-hosted microscopic pores are relatively developed and locally orientated parallel/sub-parallel to the mudstone/shale bedding (Fig. 5a). This coincides with type II_2 kerogen occurrence (Fig. 4b; Gao et al., 2016). The observed bitumen pores in argillaceous reservoirs of the Xu3 (T_3x^3) and Xu5 (T_3x^5) members play a positive role in the development of hydrocarbon storage spaces.

4.4.5. Micro-fractures

Micro-fractures are typically associated with internal stress generated by dehydration, drying shrinkage, mineral recrystallization, and hydrocarbon generation in continental shale reservoirs during burial and diagenesis. A large number of micro-fractures are widely distributed across the matrixes of inorganic (especially calcareous) grains and organic matter laminations, appear along the boundary between organic matter and minerals and are found within the framework of clay flakes in Upper Triassic Xujiahe continental shales (Fig. 5c). These observed microfractures appear to interconnect micropore spaces and thus may increase the seepage capacity of continental shale by forming pore networks.

4.5. Whole-aperture pore structures of the Xujiahe continental shale units

Before collecting measurements of reservoir physical properties (Figs. 6 and 7), whole-aperture pore-structure characterization was conducted (Figs. 8–11). Curves of mercury intrusion and evacuation and low-pressure N_2 adsorption-desorption isotherms of Xujiahe continental fine-grained sediments generally show similar behaviors. According to the IUPAC's classification, the shapes of hysteresis loops in the experimental samples are similar to those of type H3, indicating the presence of slit-like pores. A plot of dV (pore volume)/dD (pore diameter) versus D for N_2 is used to illustrate the microscopic mesopore size distribution (Rouquerol et al., 1994; Chalmers et al., 2012; Tian et al., 2013; Yang et al., 2018) and to compare relative mesopore volumes and mesopore surface areas across pore size ranges. Most peak pore sizes are identified to range from 5 to 8 nm, suggesting that mesopores within this radii interval dominate (Fig. 9).

A multimodal distribution of micropore pore volumes and surface areas with pore size can be identified from low-pressure CO_2 adsorption results based on the DFT model, exhibiting peak values at pore diameters of approximately 0.35 nm, 0.46 nm, 0.50 nm, 0.57 nm, 0.63 nm and 0.82 nm and suggesting that micropores centring on these radii dominate (Fig. 10).

From the varying ranges and accuracy of characteristics of micro-, meso-, and macropores, based on a combination of low-pressure CO_2 adsorption, low-pressure N_2 adsorption, and high-pressure mercury adsorption, the whole-aperture distribution of pore volumes and surface areas of Upper Triassic Xujiahe continental shales is displayed below (Fig. 11). The statistics show that micro- and mesopores contribute significantly while macropores play a relatively minor role in the total pore surface area. By contrast, meso- and macropores constitute most of the pore volume while micropores are less common (Fig. 11).

It is worth to stressing that the multi-scale pore volume and specific surface area of the studied mudstones/shales are significantly higher than those of silty mudstones, especially within the range of micro- and mesopore-size intervals (Fig. 11). More specifically, for micro- and mesopores, from our analysis of combined N_2 and CO_2 gas adsorption data using calculation models and applying density function theory (DFT) and Dubinine-Radushkevich (DR), the average pore volumes (0.033 and

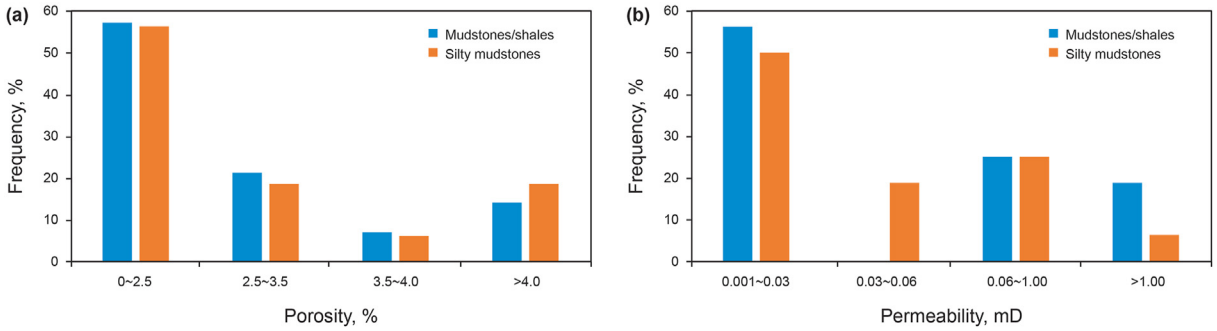

Fig. 6. The measured porosity (a) and permeability (b) distributions of different ranges of the argillaceous and silty mudstone sediments in the Xu3 (T_3x^3) and Xu5 (T_3x^5) members of the Upper Triassic Xujiahe Formation.

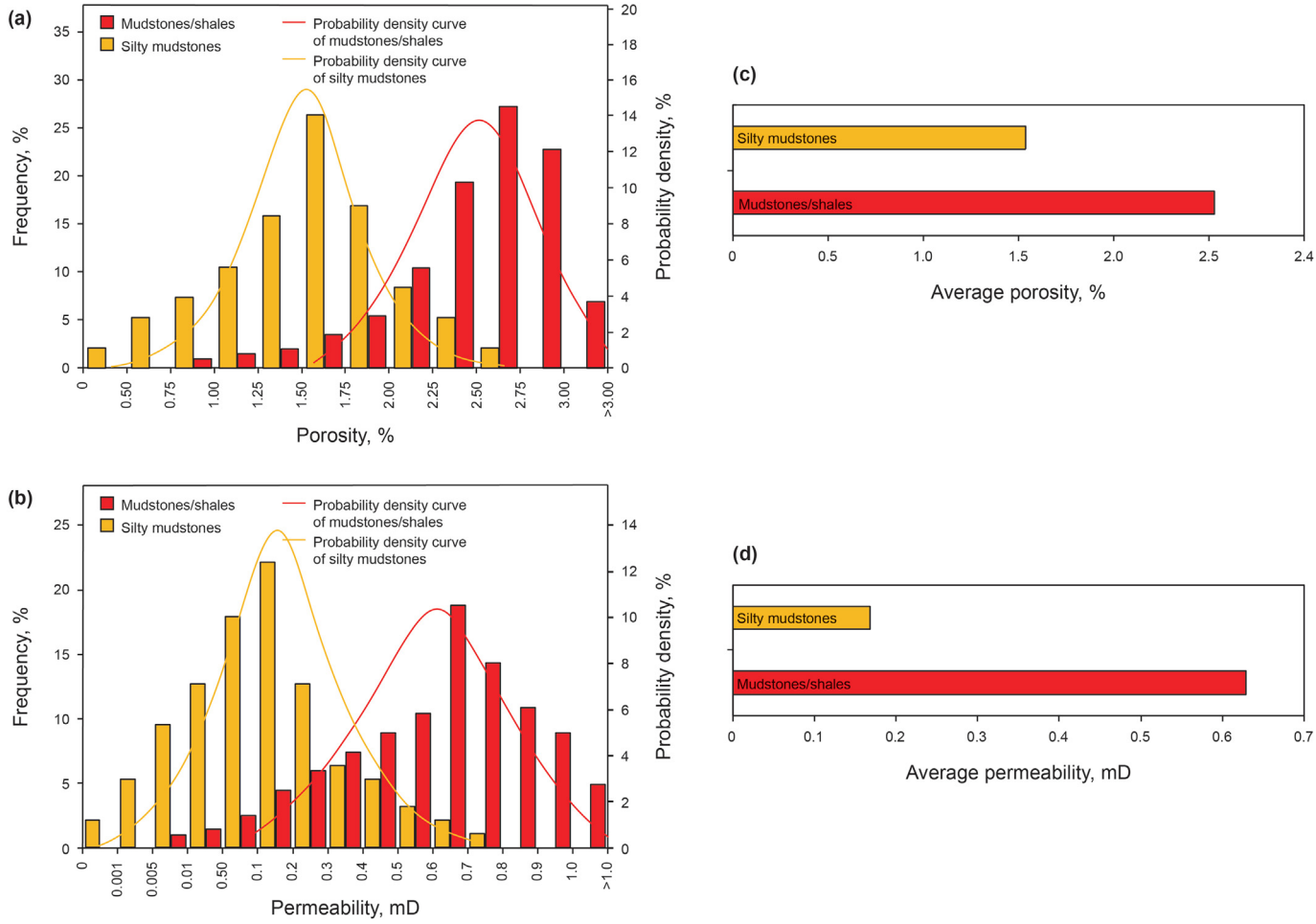

Fig. 7. (a, b) Histograms of measured porosity and permeability values respectively, of the selected Xu3 (T_3x^3) — Xu5 (T_3x^5) argillaceous and silty mudstone samples from other adjacent cored well sites (well sites X 503 (e.g., Chen et al., 2016a), XY HF-1, and XY HF-2). The X-axis shows the measured physical properties ranges, the left Y-axis displays the porosity/permeability frequency (%), and the right Y-axis indicates the probability density for the individual measurement intervals (%). (c, d) Comparison of average porosity and permeability values from the mudstone/shale and silty mudstone reservoirs. The significant superiorities of physical properties in the argillaceous sediments are also visible.

0.004 cc/g, respectively) and especially specific surface areas (11.58 and 11.91 m^2/g, respectively) of mudstones/shales are higher than those of silty mudstones, yielding values of 0.027 and 0.003 cc/g, and 8.82 and 9.01 m^2/g, respectively (Table 4). However, this work do not find macropore volumes and specific surface areas of the mudstones/shales to be superior to those of the silty mudstones (Figs. 8 and 11), as the same average values of 0.003 cc/g and 0.08 m^2/g, respectively, are found for both of these two lithological categories. This important phenomenon deserves special attention in geological reservoir research.

4.6. Physical properties of Xujiahe continental shale units

A systematic petrophysical analysis of continental silty-mud

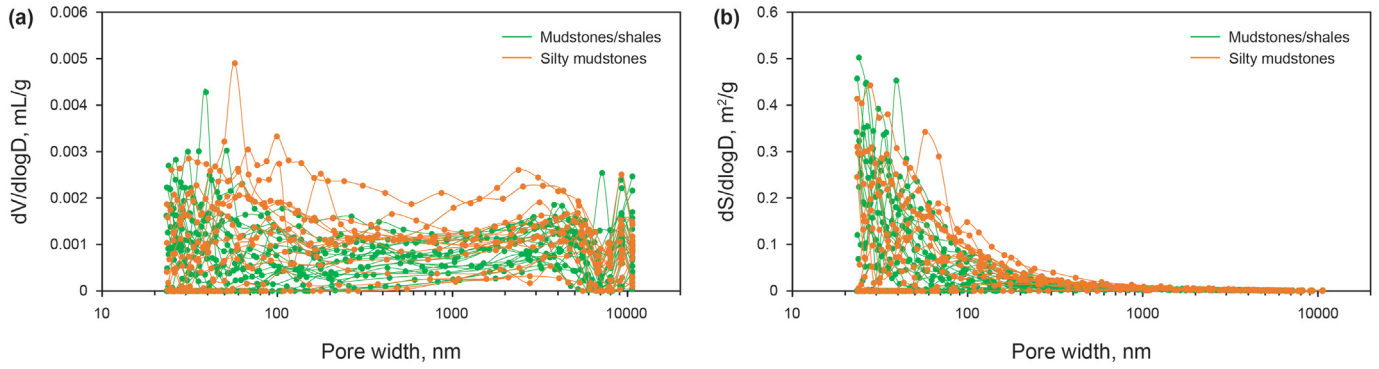

Fig. 8. Macropore volume (a) and surface area (b) distributions obtained via high-pressure mercury injection respectively for the mudstones/shales and silty mudstones of the Xu3 (T_3x^3) and Xu5 (T_3x^5) members deposited in the Upper Triassic Xujiahe Formation.

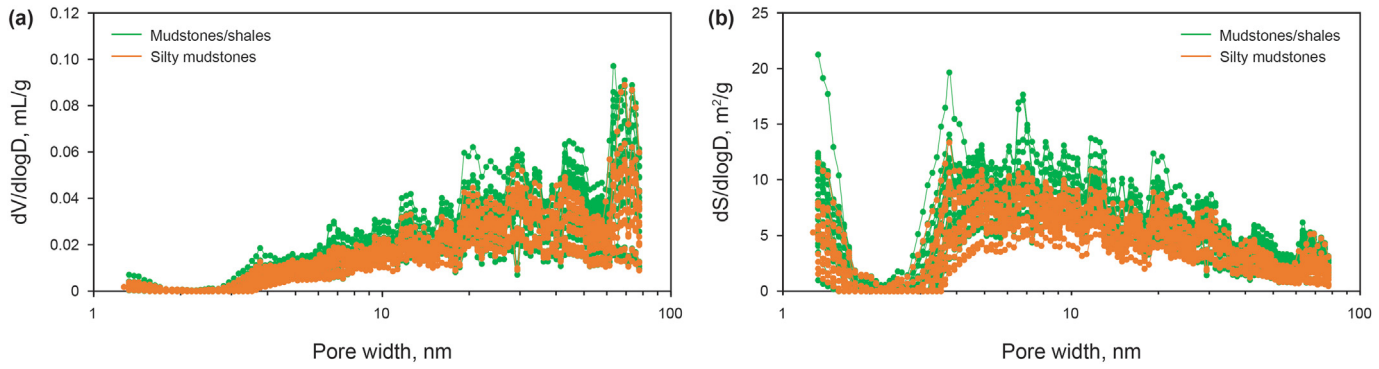

Fig. 9. Mesopore size distributions obtained by N_2 adsorption analysis respectively for the mudstones/shales and silty mudstones of the Xu3 (T_3x^3) and Xu5 (T_3x^5) members deposited in the Upper Triassic Xujiahe Formation. (a) Mesopore size distribution with respect to pore volume; (b) Mesopore size distribution with respect to pore surface area.

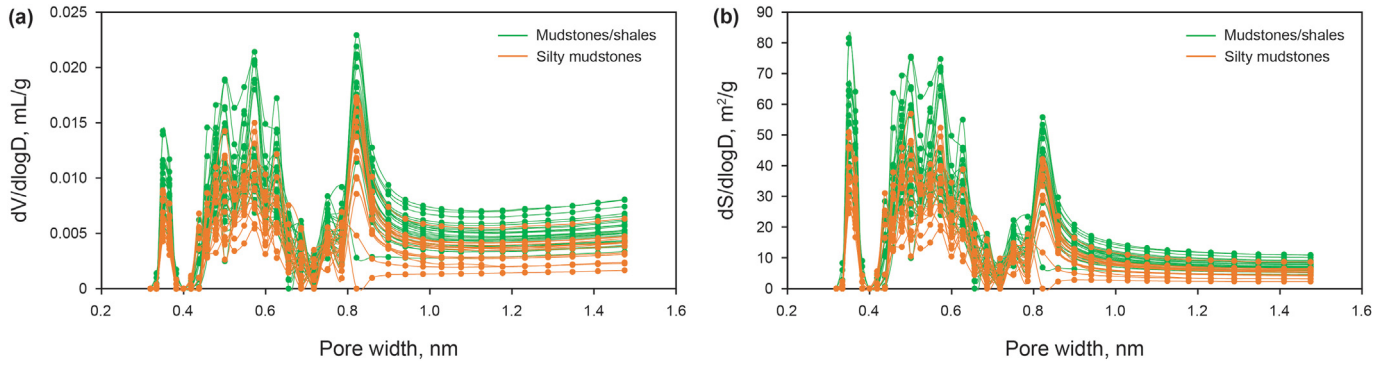

Fig. 10. Micropore size distributions obtained by CO_2 adsorption analysis respectively for the mudstones/shales and silty mudstones of the Xu3 (T_3x^3) and Xu5 (T_3x^5) members deposited in the Upper Triassic Xujiahe Formation. (a) Micropore size distribution with respect to pore volume; (b) Micropore size distribution with respect to pore surface area.

sediments of the targeted cored Well Ledi 1 show that porosity ranges from 1.1% to 6.0% with an average value of approximately 2.8% while permeability varies from 0.002 to 0.400 mD, yielding a mean value of 3.190 mD (Table 5). In detail, mudstones/shales exhibit higher average porosity parameters than silty mudstones, and more specifically, respectively lie in 2.76% and 2.71% for porosity and 0.546 mD and 0.163 mD for permeability in terms of these two lithological categories (Table 5). Additionally, mudstones/shales display a higher proportion of physical properties than silty mudstones within main and specific ranges of 0–2.5%, 2.5–3.5%, and 3.5–4% for porosity and 0.001–0.03 mD, 0.03–0.06 mD, 0.06–1 mD, and >1 mD for permeability, respectively (Fig. 6 and Table 5). These statistical and uncommon presences drawn above are speculated to be geologically meaningful.

This is also consistent with physical property measurements of coeval silty-mud sediments from the Xu3 (T_3x^3) and Xu5 (T_3x^5) members in cored wells situated in the northern part of the western subsiding Sichuan Basin, including well sites X503 (e.g., Chen et al., 2016a), XY HF-1, and XY HF-2 (Fig. 7). Based upon a relatively large body of collected data, both the distribution frequency (Fig. 7a and b) and averages (Fig. 7c and d) imply the presence of considerably superior porosity and permeability in the argillaceous sediments.

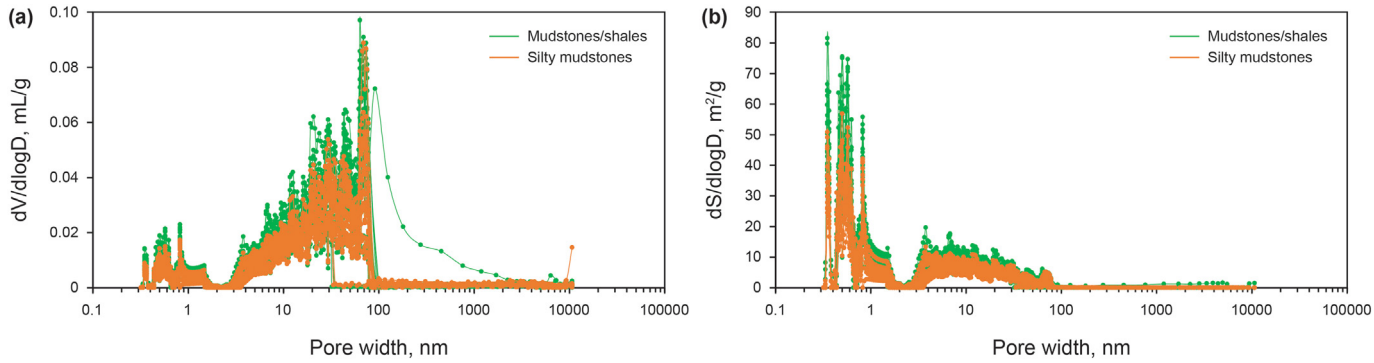

Fig. 11. Whole-aperture pore-size distribution with respect to pore volume (a) and surface area (b) of the mudstone/shale and silty mudstone reservoirs, respectively, of the Xu3 (T_3x^3) and Xu5 (T_3x^5) members deposited in the Upper Triassic Xujiahe Formation.

5. Discussion

5.1. Favorable physical properties and pore structures of mud-shale sediments

To our knowledge, in the case of fine-grained sedimentary rocks with similar categories of microfacies (lithofacies) or diagenetic facies, the effect of granularity on petrophysical properties is significant and characterized by relatively high porosity-permeability in silty mudstones compared to mudstones/shales (Yin, 2003; Aplin and Macquaker, 2011; Milroy et al., 2019). The correlation coefficients between granularity and porosity and permeability are 0.5 and 0.52, respectively, taking fine-grained fluvio-lacustrine deposits of the Yanchang Formation in the Late Triassic Ordos Basin of central China as an example (Yin, 2003; Zhang, 2005). Nevertheless, the principal features pertain to the excellent positive covariance of grain size and permeability with regard to homogeneous lithofacies (Yang & Aplin, 1998, 2007; 2007; Wang, 2007) and an exponential decrease in permeability as lithofacies type converted fine-grained sandstones into argillaceous rocks (Wan et al., 2018). Additionally, a quantitative analysis of equivalent grain sizes in fine-grained delta front deposits exhibited that differences in granularity may lead to an approximately twofold gap in the theoretical value of permeability (Sneider et al., 1978; Fu et al., 2013; Jin et al., 2016).

Another prevailing view concerns the microscopic pore structure properties of fine-grained sediments. Effects of granularity on macropore structure characteristics clearly exists exhibiting significantly better pore structures in silty mudstones than in mudstones/shales in respect of continental fine-grained deposits (Xu et al., 2013; Li et al., 2019). In the case of the Eocene Shahejie argillaceous sediments from the Bohai Bay Basin in eastern China, macropore volumes and connectivity decrease and become less orderly with variations in lithofacies from argillaceous siltstones, silty mudstones, and mudstones/shales (Xu et al., 2013; Xu, 2014; Li et al., 2019).

Nevertheless, as reported above, in terms of the physical properties of Xujiahe silty-mud units, the greatly significant advantage for mudstones/shales corresponds to a notable threefold increase in average permeability relative to silty mudstones. In addition, a slight enhancement in reservoir porosity is meanwhile identified and non-negligible for Upper Triassic Xujiahe continental mudstones/shales. Further detailed investigations on the multi-stage distribution of reservoir property within specific ranges show that mudrocks present a significant advantage over silty sandstones in average permeability within ranges of greater than 0.06 mD, whereas average values of porosity are generally well matched between these two representative lithofacies as featured by superiorities prevailing at intervals of 0–2.5%, 2.5–3.5%, and 3.5–4%, respectively (Fig. 6). The generally better permeability detected from the investigated continental mudrocks leads to superior reservoir performance as characterized by the extensive development of relatively large, interconnected, and effective pore spaces, and even by the presence of polygenetic micro-fractures serving as migration pathways through shale-gas systems, favorable for the occurrence and storage of free gas (Liang et al., 2014; He et al., 2016; Lai et al., 2018).

In addition, as reported above, in terms of the microscopic pore structure characteristics of Xujiahe silty-mud units, mudstones/shales make significant contributions to specific surface area and also provide a relatively larger volume than silty mudstones (Fig. 11). This trend agrees with the measurement of petrophysical properties characterized by substantially higher permeability and porosity, respectively. Thus, the heterogeneous reservoir properties of Upper Triassic Xujiahe silty-mud sediments cannot be ignored, and continental Xujiahe mudstones/shales can provide more excellent reservoir space for storage sites of adsorbed gas, permeable migration pathways, and potential seepage channels of shale gas (Slatt & O'Brien, 2011; Chen et al., 2016a; 2019; Liu et al., 2017).

5.2. Contributors to micro-reservoir space particularity in the Xujiahe silty-mud units

5.2.1. Organic-hosted (especially bitumen) pores

Commonly occurred organic matter pores are largely regarded as the dominant pore type and play a significant role in the development and distribution of microscopic pore systems in marine shales (Loucks et al., 2009; Milliken et al., 2013; Gao et al., 2018). However, organic pores have also been confirmed to make non-negligible contributions to reservoir space in certain fluvio-lacustrine mudstones and shales characterized by small sponge-like organic-hosted pores developing in textures composed of organic particles and clay minerals in Lower Cretaceous Shahezi shales of the southern Songliao Basin (Gao et al., 2019; Liu et al., 2019b), and by oil and gas outlet organic-hosted pores displaying bubble-like irregular shapes in Upper Triassic Yanchang shales of the southwestern Ordos Basin, China (Cao and Zhou, 2015; Yang et al., 2018).

In examining the investigated continental mudstones and shales of the Upper Triassic Xujiahe Formation in the western subsiding Sichuan Basin, FE-SEM observations with energy-dispersive spectrometry (EDS) analyses indicate that bitumen pores make major contributions to organic-related pores dispersedly but extensively distributed in different forms and shapes (Fig. 12). More specifically,

Table 4
The collected statistics of the pore volume (PV) and surface area (PSV) data determined by high-pressure mercury injection, low-pressure N_2 and CO_2 adsorption, focusing on the argillaceous and silty mudstone reservoirs of the Xu3 (T_3x^3) and Xu5 (T_3x^5) members in the Upper Triassic Xujiahe Formation.

Sample	Lithology	Depth, m	MIP		N_2 adsorption		CO_2 adsorption		Total PV. cm^3/g	Total PSA, m^2/g
			Macro PV, cm^3/g	Macro PSA, m^2/g	Meso PV, cm^3/g	Meso PSA, m^2/g	Micro PV, cm^3/g	Micro PSA, m^2/g		
LD-2	Mudstones/shales	1163.38	0.0102	0.5000	0.0022	7.4177	0.0039	11.4727	0.0163	19.3904
LD-7	Mudstones/shales	1168.38	0.0136	0.7011	0.0025	7.9317	0.0033	10.1489	0.0194	18.7817
LD-13	Mudstones/shales	1174.38	0.0016	0.0136	0.0009	5.8164	0.0029	9.0908	0.0054	14.9207
LD-25	Mudstones/shales	1186.40	0.0100	0.5103	0.0018	5.7866	0.0035	10.4297	0.0154	16.7266
LD-29	Mudstones/shales	1192.40	0.0133	1.1140	0.0022	6.5219	0.0034	9.9899	0.0189	17.6257
LD-31	Mudstones/shales	1199.40	0.0109	0.5953	0.0026	8.6852	0.0042	13.4835	0.0178	22.7639
LD-38	Mudstones/shales	1222.40	0.0085	0.5040	0.0025	7.7910	0.0040	12.6677	0.0150	20.9626
LD-61	Mudstones/shales	1241.40	0.0093	0.4658	0.0023	7.9097	0.0036	11.3208	0.0152	19.6962
LD-80	Mudstones/shales	1251.40	0.0110	0.5930	0.0023	7.3055	0.0029	9.0642	0.0163	16.9626
LD-90	Mudstones/shales	1163.38	0.0044	0.1675	0.0017	7.5198	0.0033	11.1274	0.0093	18.8146
LD-111	Mudstones/shales	1272.30	0.0129	0.7135	0.0033	10.7452	0.0041	12.0152	0.0202	23.4739
LD-118	Mudstones/shales	1279.30	0.0075	0.3216	0.0021	8.1210	0.0042	12.9155	0.0138	21.3581
LD-129	Mudstones/shales	1290.30	0.0022	0.0227	0.0013	8.2112	0.0054	16.5221	0.0089	24.7560
LD-151	Mudstones/shales	1350.50	0.0055	0.2104	0.0018	7.3671	0.0038	11.7196	0.0111	19.2970
LD-156	Mudstones/shales	1378.10	0.0100	0.4505	0.0017	5.6351	0.0030	9.1268	0.0147	15.2123
LD-167	Mudstones/shales	1389.10	0.0140	0.6939	0.0031	10.9411	0.0058	17.9969	0.0229	29.6318
LD-170	Mudstones/shales	1392.10	0.0057	0.2965	0.0020	7.8811	0.0042	12.7624	0.0119	20.9400
LD-177	Mudstones/shales	1400.10	0.0125	0.6273	0.0024	7.8986	0.0036	11.3951	0.0185	19.9210
LD-191	Mudstones/shales	1418.10	0.0098	0.4864	0.0020	6.6880	0.0038	11.7778	0.0156	18.9521
LD-197	Mudstones/shales	1353.00	0.0048	0.1978	0.0017	7.6024	0.0030	9.4625	0.0096	17.2627
LD-200	Mudstones/shales	1359.00	0.0078	0.4605	0.0024	8.2889	0.0049	15.5637	0.0151	24.3131
LD-215	Mudstones/shales	1429.70	0.0085	0.3769	0.0020	7.5953	0.0041	12.6372	0.0147	20.6094
LD-216	Mudstones/shales	1431.70	0.0016	0.0171	0.0014	9.2828	0.0050	15.5447	0.0080	24.8446
LD-217	Mudstones/shales	1433.70	0.0105	0.5959	0.0022	7.3445	0.0061	19.5343	0.0188	27.4746
LD-231	Mudstones/shales	1456.70	0.0154	0.7587	0.0028	9.3970	0.0048	14.7142	0.0230	24.8699
LD-22	Silty mudstones	1183.40	0.0020	0.0254	0.0010	6.1778	0.0031	9.2179	0.0061	15.4211
LD-50	Silty mudstones	1211.40	0.0113	0.5411	0.0020	6.2069	0.0029	8.8713	0.0162	15.6192
LD-78	Silty mudstones	1239.40	0.0084	0.3726	0.0017	5.3607	0.0022	7.2273	0.0123	12.9605
LD-82	Silty mudstones	1243.40	0.0116	0.6072	0.0022	6.6663	0.0029	9.0978	0.0168	16.3714
LD-85	Silty mudstones	1246.40	0.0065	0.2599	0.0012	3.7827	0.0014	4.6843	0.0092	8.7269
LD-96	Silty mudstones	1257.40	0.0056	0.2714	0.0014	4.9089	0.0022	6.7962	0.0091	11.9764
LD-105	Silty mudstones	1266.40	0.0077	0.4598	0.0025	8.0185	0.0026	7.7313	0.0129	16.2095
LD-133	Silty mudstones	1294.30	0.0098	0.4353	0.0021	6.6729	0.0033	10.0182	0.0152	17.1264
LD-149	Silty mudstones	1348.50	0.0052	0.2813	0.0016	5.3246	0.0025	7.5970	0.0092	13.2029
LD-162	Silty mudstones	1384.10	0.0055	0.2487	0.0015	6.0842	0.0035	10.8746	0.0105	17.2074
LD-173	Silty mudstones	1396.10	0.0094	0.4909	0.0021	7.0070	0.0032	10.3856	0.0147	17.8835
LD-201	Silty mudstones	1360.00	0.0080	0.2325	0.0015	6.3940	0.0034	10.5835	0.0129	17.2099
LD-206	Silty mudstones	1368.10	0.0117	0.5456	0.0021	7.5282	0.0036	11.1537	0.0174	19.2274
LD-210	Silty mudstones	1373.10	0.0080	0.4667	0.0021	6.7930	0.0035	10.8952	0.0136	18.1549
LD-224	Silty mudstones	1445.70	0.0078	0.3351	0.0020	7.6725	0.0042	13.0159	0.0140	21.0235
LD-235	Silty mudstones	1462.70	0.0037	0.0465	0.0011	7.0880	0.0037	11.6830	0.0085	18.8175

Table 5
The statistics of measured permeability and porosity of the tested Xu3 (T_3x^3) — Xu5 (T_3x^5) mudstones/shales and silty mudstones sampled from the cored Well Ledi 1.

Sample	Lithology	Depth, m	Porosity, %	Permeability, mD
LD-1	Mudstones/shales	1162.40	1.6	0.0026
LD-25	Mudstones/shales	1186.40	4.8	0.5588
LD-43	Mudstones/shales	1204.40	2.3	0.1604
LD-80	Mudstones/shales	1241.40	1.9	0.0080
LD-88	Mudstones/shales	1249.40	1.1	0.0202
LD-111	Mudstones/shales	1272.30	2.8	0.3223
LD-126	Mudstones/shales	1287.40	1.7	0.0116
LD-167	Mudstones/shales	1389.10	2.1	0.0083
LD-177	Mudstones/shales	1400.10	2.4	0.0045
LD-179	Mudstones/shales	1402.10	6.0	0.0051
LD-191	Mudstones/shales	1418.10	1.7	0.0019
LD-215	Mudstones/shales	1429.70	2.9	0.0051
LD-236	Mudstones/shales	1463.70	3.4	0.6390
LD-237	Mudstones/shales	1464.70	3.9	3.1900
LD-14	Silty mudstones	1175.40	1.4	2.6300
LD-22	Silty mudstones	1183.40	2.2	0.0015
LD-33	Silty mudstones	1194.40	1.4	0.0044
LD-50	Silty mudstones	1211.40	2.1	0.0471
LD-72	Silty mudstones	1233.40	2.1	0.0623
LD-78	Silty mudstones	1239.40	1.5	0.0350
LD-82	Silty mudstones	1243.40	4.3	0.0225
LD-99	Silty mudstones	1260.40	5.7	0.0125
LD-105	Silty mudstones	1266.40	2.0	0.0494
LD-109	Silty mudstones	1270.30	2.1	0.1265
LD-133	Silty mudstones	1294.30	2.6	0.0055
LD-145	Silty mudstones	1344.50	3.1	0.1214
LD-173	Silty mudstones	1396.10	5.5	0.0023
LD-206	Silty mudstones	1368.10	2.2	0.0044
LD-209	Silty mudstones	1372.10	3.6	0.0059
LD-234	Silty mudstones	1460.70	2.9	0.0785

the main prevailing type exhibits strong anisotropy and is characterized by irregular/elliptical pores occurring mostly along the edges of brittle mineral grains positioned adjacent to the centre or along the margins of bitumen residues/primary organic matter (Fig. 12a and b). Another development mode frequently observed concerns clay-organic complexes of even nanocomposites consisting mainly of authigenic clay layers and bitumen residues (Schulten et al., 1996; Kennedy et al., 2014; Yang et al., 2018), featured by organic matter masses either attached to crystal surfaces of clay sheets or obliquely penetrated by clay layers (Fig. 12c, d, e and f; Schulten et al., 1996; Rahman et al., 2017). The associations of detrital clays contained in bitumen residues (Fig. 12c, d and e) and bitumen veins sandwiched between individual clay laminae also deserve special attention (Fig. 12f and g). Additionally, shrinkage cracks and shrinking pores forming within organic matter masses and between organic matter and clay/brittle minerals make relatively strong contributions to reservoir quality (Fig. 12h, k and n). Observations demonstrate that the elongated and evenly positioned micropore-fracture system grows along the edges of bitumen residues taking dominately the morphology of long strips or curly flakes between clay crystal aggregates due to shrinkage processes, prevailing in lacustrine shales and marked by high concentrations of clay minerals and well-formed horizontal bedding planes in multilayer sequences (Fig. 12d, h, i, g and 13; Chalmers et al., 2012; Ougier-Simonin et al., 2016; Yang et al., 2019c; Jiang et al., 2018). This echoes the features of nanoscale storage spaces found in the lacustrine and laminated shales of the Lower Cretaceous Shahezi Formation deposited in the faulted Songliao Basin (NE China), which are characterized by the development of oriented organic pores occurring in organic matter along strip-like chlorite assemblages (Yawar and Schieber, 2017; Gao et al., 2018; Liu et al., 2019b). The presently studied and previously reported cases are thus in accordance with fluvio-lacustrine reservoir characteristics of the enrichment of liquid hydrocarbons and bitumen, which can be attributed to the relatively low thermal evolution degree of continental mudstones/shales (Lai et al., 2015; Yang et al., 2019c).

The shrinkage of organic matter during hydrocarbon expulsion and degradation contributes significantly to microcracks formation along bedding planes and bitumen pores elongated between similarly oriented clay sheets (Fig. 12a, h, i, j, k, l and n; Ougier-Simonin et al., 2016; Wang and Guo, 2019). Interconnections and the even penetration of these microcracks and bitumen pore-associated bedding fractures benefit the formation of micro-bedding fractures alongside bedding surfaces (planes) positioned horizontally or at a low angle (Fig. 12k, m and o; He et al., 2017; Lyu et al., 2017; Zhang et al., 2017; Li et al., 2018). Furthermore, the aforementioned mechanisms are believed to facilitate the formation and development of non-bedding microfractures extending in multiple directions (Fig. 12o and p).

Bedding and interlayer cracks typically form along sedimentary bedding structures and horizontally weak planes of continental mudstones/shales, significantly contributing to the expansion of reservoir spaces and even acting as critical channels for fluid migration and flow (Fig. 12; Dewhurst et al., 2011; He et al. 2011; Ding et al., 2013; Zhang et al., 2019). Considering their considerable effects in improving physical properties, and reservoir permeability in particular, bedding fractures serve not only as excellent reservoirs but also as connected and effective pathways for continental shale gas storage and transmission (Wang et al., 2018; Liu, 2019). Another peculiar aspect, bedding fractures are widely known to occur in association with high-angle natural fractures mostly formed through tectonic deformation, facilitating the formation and broad distribution of interwoven fracture and pore-fracture networks and enhancing storage spaces and seepage capacity (Fig. 12; Xu et al., 2008; Ferrill et al., 2014; Zhang et al., 2017; Su et al., 2018). Besides, non-bedding microfractures may have a similar effect on the formation and development of oblique natural fractures, also exerting positive control over the quality of continental shale reservoirs (He et al., 2017; Dong et al., 2018).

5.2.2. Clay minerals

It is important to stress that differences in the concentrations of clay minerals between silty mudstones and mudstones/shales are significant (Fig. 2 and Table 1). It is also evident from our detailed FE-SEM observations that inter-crystalline pores well-developed in clay minerals mainly occur along grain aggregates and between similarly oriented platelets (Fig. 13), in view of a characteristic bended and intermittent morphology, a relatively higher concentration of filled interdetrital matrix, and an significantly lower average width/opening of the gaps (microcracks) between clay pieces (Chen et al., 2013; Qian et al., 2017; Guo et al., 2020). The morphologies of identified clay inter-crystalline pores can be distinguished as two main types: (1) *Type 1* generally features elongated and compressed linear shapes mainly due to the lamellar/filiform texture of illites and the flocculated structure of illite-smectite mixed-layers, and occasionally booklet/accordion-like chlorites/deformed kaolinites (Fig. 13a and b). Widespread and reticular *Type 1* pore systems manifested by higher reservoir capacities and better connectivity, are usually considered to have arisen from the interconnection of inter-crystalline pores along surfaces of clay sheets, favorable for the development of bedding/non-bedding microfractures, which serve as effective hydrocarbon infiltration channels (Fig. 13b, e, f and h; Wang et al., 2015; Xue et al., 2015; Chen et al., 2016b; Sun and Guo, 2016). Alternatively, complex network systems can form through associations between clay inter-crystalline and residual intergranular pores, which also facilitates the generation of microcracks and greatly improves

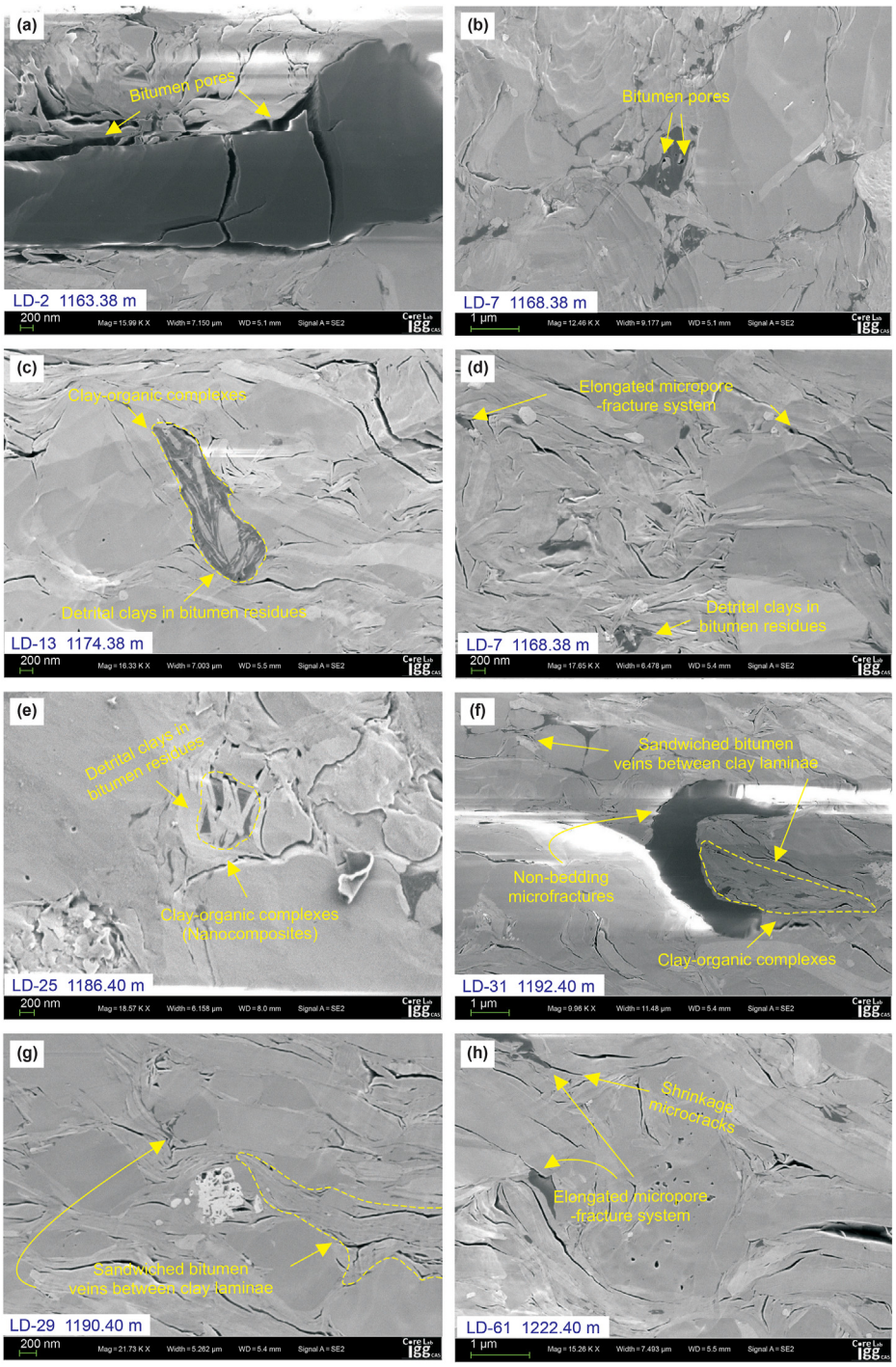

Fig. 12. Characteristic FE-SEM images mainly showing development and distribution of bitumen-associated pores, and concomitant micropore-microfracture and bedding/non-bedding microfracture systems developed in the investigated mudstone/shale reservoirs. (a, b) Characteristic bitumen pores occurring along the margins or at the edge of brittle mineral grains positioned adjacent to centre of bitumen residues/primary organic matter; (c, d, e) Common occurrence of bitumen-associated pores developed in clay-organic complexes constituting nanocomposites locally, particularly characterized by detrital clays in bitumen residues and also elongated micropore-microfracture system occasionally; (f, g, h) Pores distributed in sandwiched bitumen veins occurring between clay lamiane, and clay-organic complexes and non-bedding microfractures taking dominately the morphology of marginal bitumen pores are also observed. (i, j) Typical occurrence of micropore-microfracture systems favorable for creation of bedding-parallel microfractures; (k, l, m, n) Representative occurrence of micro bedding fracture systems formed mainly as the result of interconnection, penetration, as well as interwoven configuration of shrinkage microcracks; (o, p) Co-occurrence of micro bedding and non-bedding fracture systems, and characteristic bitumen pores-associated oblique fractures are visible.

storage and seepage capacities and the overall quality of fluvio-lacustrine mudstone/shale reservoirs (Fig. 13g; Jin et al., 2015; Nole et al., 2016; Sun and Guo, 2016). (2) *Type 2* appears to be triangular or irregularly polygonal in morphology (Fig. 13b, c and d) and exhibits characteristics including larger storage spaces but poorer connectivity and permeable pathways in pore systems than those

of *Type 1* due to the presence of significantly higher pore diameters (equivalent circular diameters), and more enclosed/semi-restricted individual pore spaces with gradual pinchout boundaries, respectively (Fig. 13b, c and d; Li et al., 2017). Nevertheless, in the case of occurrences adjacent to terminations of individual microcracks, *Type 2* pores can make a relatively substantial contribution to the total extensional length and fracture scale of associations of oriented microfractures and help improve the percolation capacity of argillaceous reservoirs to some degree (Fig. 13b). Thus, taking Xu3 (T_3x^3) and Xu5 (T_3x^5) mudstone/shale units of the Upper Triassic Xujiahe Formation as an example, significant effects of high clay mineral enrichment on reservoir properties and quality are elucidated and emphasized. This is also supported by the significant impact of intergranular pores parallel to the long axes of clay tablets/occurring between clay aggregates observed in the Mesozoic Shahezi shales mentioned above (Wei et al., 2010; Liu et al., 2019b).

5.3. New insights into a differential reservoir-forming model for silty-mud sediments

The lithological association between interlayered silty mudstones and mudstones/shales of the Upper Triassic Xujiahe

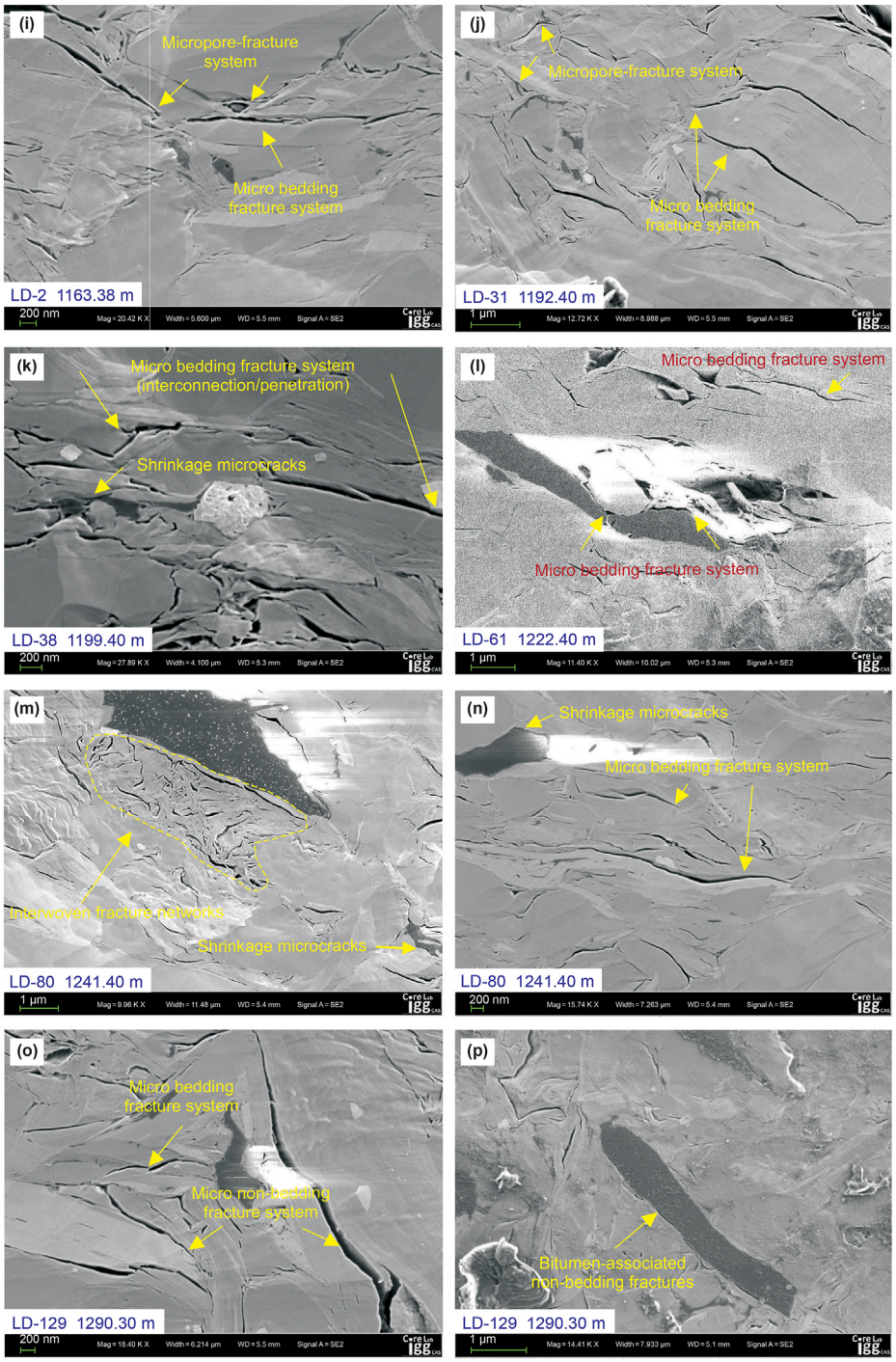

Fig. 12. (*continued*).

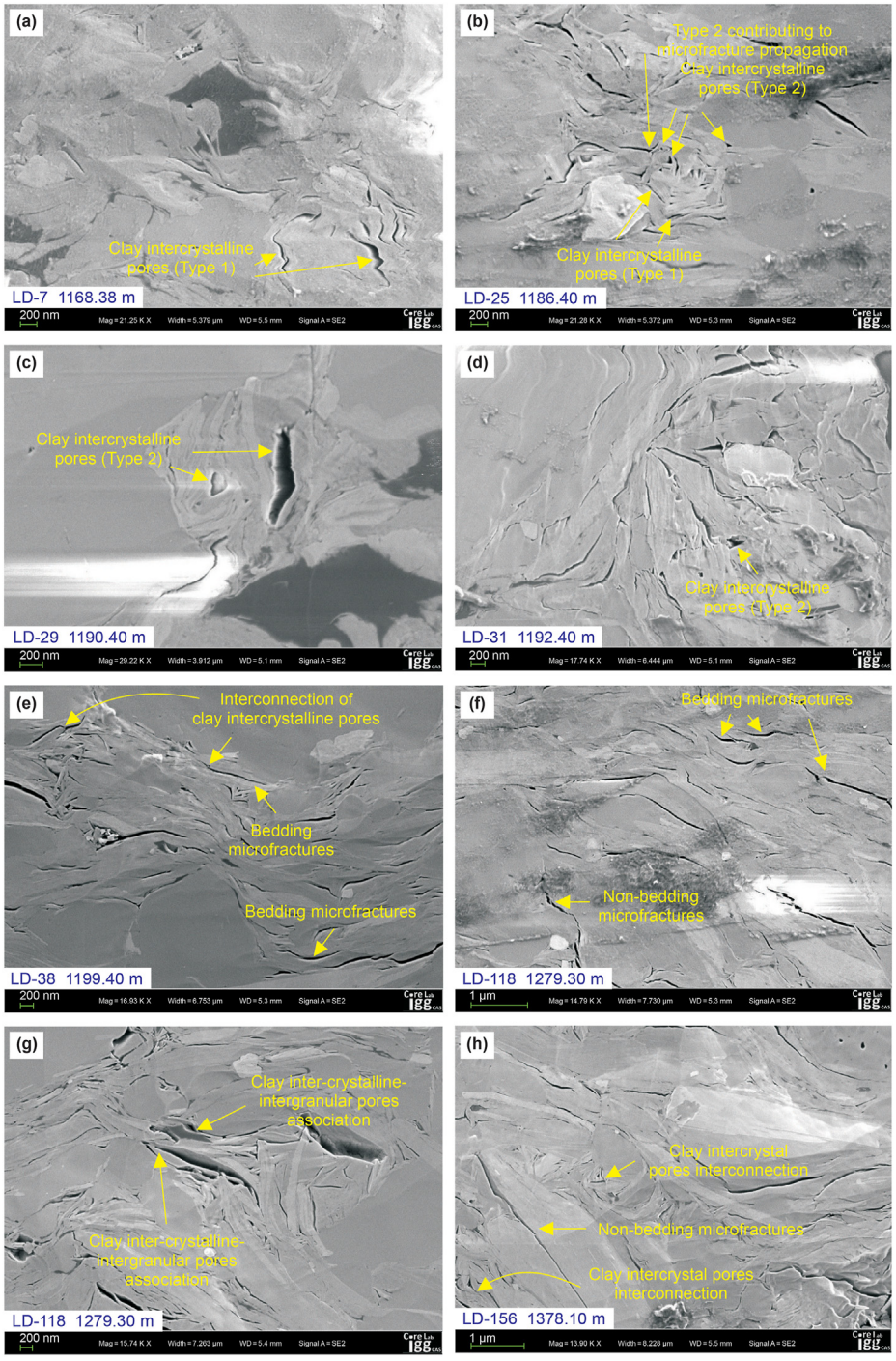

Fig. 13. Characteristic FE-SEM images mainly displaying development, interconnection, and associations of the two typical categories of inter-crystalline pores, and concomitant micropore-microfracture and bedding/non-bedding microfracture systems identified in the investigated mudstone/shale reservoirs. (a) *Type 1* of clay inter-crystal pores featured by elongated and compressed linear shapes formed as a result of characteristic structure/texture of clay mineral admixtures; (b, c, d) *Type 2* of clay inter-crystal pores appears to be triangular or irregular polygonal in morphology characterized by enclosed/semi-restricted shapes, or occurs adjacent to terminations of individual microcracks; (e, f) Characteristics of microfractures parallel/sub-parallel to bedding-planes due to interconnections of clay inter-crystal pores, and non-bedding microfractures are also observed; (g, h) Characteristics of non-bedding microfractures due to interconnections of clay inter-crystal pores, and associations of clay inter-crystalline and intergranular pores.

Formation provides an ideal basis and valuable archives for investigating potential causes for the improvement in reservoir properties found in the Xujiahe mud-shale sediments.

Both the silty mudstones and mudstone/shale reservoirs in the shale-dominated Xu3 (T_3x^3) and Xu5 (T_3x^5) members of the continental Xujiahe Formation have encountered the same burial diagenetic regimes and processes, enabling us to conduct a comparative study to clarify and better illustrate the potential influence of granularity on reservoir properties and quality. This corresponds well with the important and continuous scientific topic that how considerable heterogeneity in internal reservoir attributes can be driven by primary sedimentary micro-textures, structures and compositions (Weber, 1986; Luo et al. 2014, 2016; 2016; Schieber et al., 2019; Li and Schieber, 2020; Luis et al., 2020).

Our investigation emphasizes the crucial importance of bitumen pores and clay minerals for improving reservoir capacity and quality, especially for remarkably enhancing permeability condition. Specifically, mudstones/shales from the argillaceous Xu3 (T_3x^3) and Xu5 (T_3x^5) members contain relatively well-developed fracture network systems constituted of numerous well-developed bedding and non-bedding microfractures spreading in multiple directions (Fig. 14a and b). This is most likely driven by the two aforementioned mechanisms concerning bitumen-hosted pores and clay inter-crystalline pores, both being more common within the micropore and mesopore size fraction. First, bitumen-hosted pores occupying most of organic matter pores mainly develop adjacent to scattered debris of inorganic minerals remaining within the bitumen particles and between sandwiched clay-organic associations that are elliptical to elongated in shape. Thermal shrinkage triggers the bedding and non-bedding shrinking microcracks with the characteristic micro-morphology of bitumen pores and subsequently for the pore-fracture structure, complex and interwoven fracture networks (Fig. 14a and b). As another striking aspect to note, well-orientated/extensively distributed inter-crystalline pores occurring predominately in illites and illite-smectite intermediates exert immense effects on the development of network systems composed of oblique microfractures with irregular occurrences. Extending along original laminated, lath-like, and sometimes triangular mineral textures, the two main categories of intercrystal pore spaces are prone to interpenetration and are effectively connected to primary intergranular pore systems (Fig. 14b). This is thus more beneficial for the enhancement of gas storage potential and percolation ability due to the formation of internally connected and intricate microfracture framework systems as thoroughly afore-documented and iconically depicted by the proposed mode illustrated in Fig. 14b. In contrast to mudstone/shale reservoirs, silty mudstones accumulate fewer organic matter particles and preserve less bitumen residues covering a wide variety of morphologies, resulting in a relatively poorer development of bitumen-hosted microscopic pores and associated microcracks than observed for the argillaceous architectural units (Fig. 14c and d). Moreover, a remarkably drastic reduction in the abundance of clay minerals would lead finally to a limited number of intercrystal pores and microcracks mainly elongated and positioned between illite (I) and mixed-layer illite-smectite (I/S) sheet aggregates. The insufficiency of effective storage spaces and seepage pathways depending largely on bedding and non-bedding microfractures is thus prominent and better understood for silty-mudstone reservoirs (Fig. 14c and d).

Besides, a quantitative image processing analysis are conducted on the FE-SEM images of the Xujiahe continental fine-grained sediments by using Image-Pro Plus (IPP) software, and the parameters of microscopic pores image processing represented by pore width, average microcrack width, and plane porosity of entire space (Phi), pores (Phi (P)) and microcracks (Phi (C)) were extracted from the FE-SEM images (Fig. 14). In detail, the total amount of pores in the representative mudstones/shale samples (972–1250, mean 1084) is considerably higher than that of the selected silty mudstone samples (216–306, mean 263), and the total amount of observed microcracks display similar distribution pattern characterized by a striking difference between the argillaceous (645–700, mean 678) and silty (170–208, mean 187) facies. More specifically, the pore width and average microcrack width of the silty-mud fine-grained sediments is predominant ranging from 10 to 50 nm, and

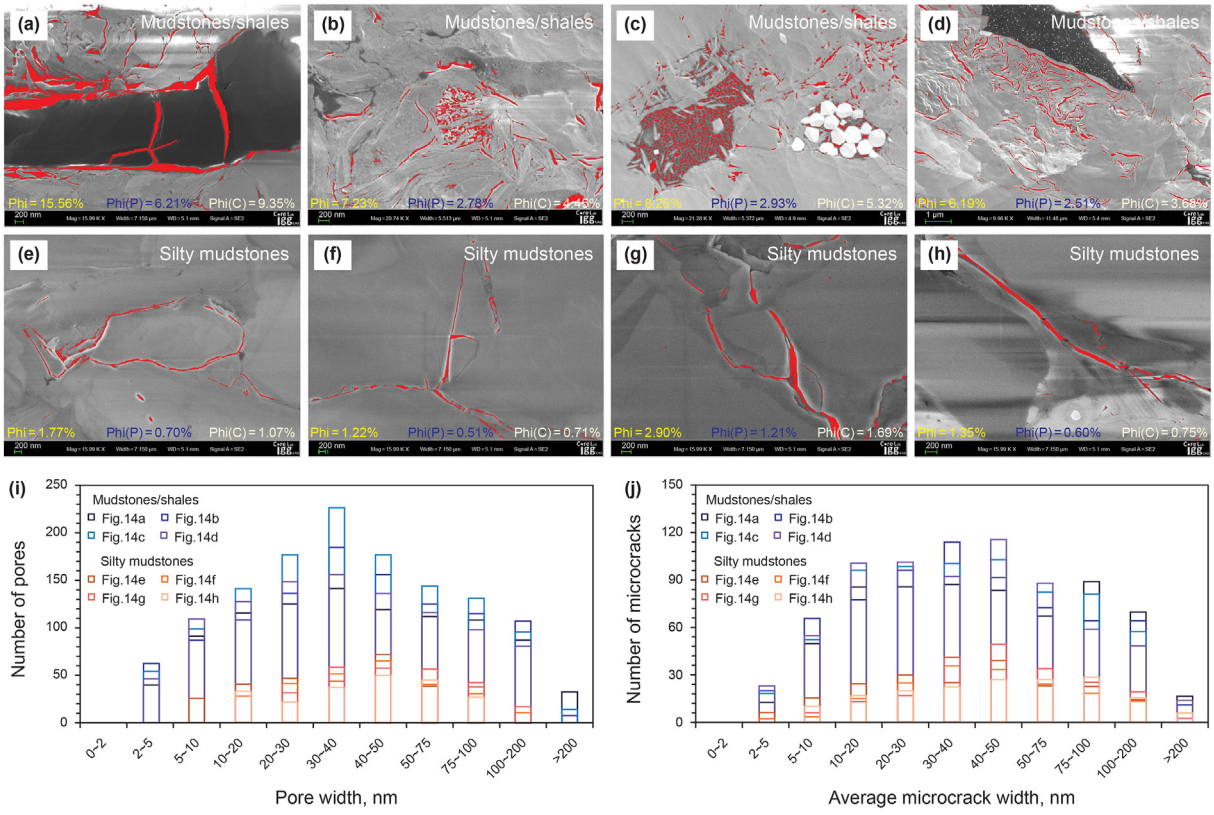

Fig. 14. Image-Pro Plus (IPP) quantitative extraction and statistics of the reservoir storage space in the representative samples of targeted silty-mud sediments. (a–h) Pores and microcracks extraction from different FE-SEM images, and the corresponding values of Phi, Phi (P), and Phi (C) are calculated. (i, j) Distribution histogram of pore and microcrack amounts for different pore width ranges for the image-extracted mudstones/shales, and silty mudstones, respectively.

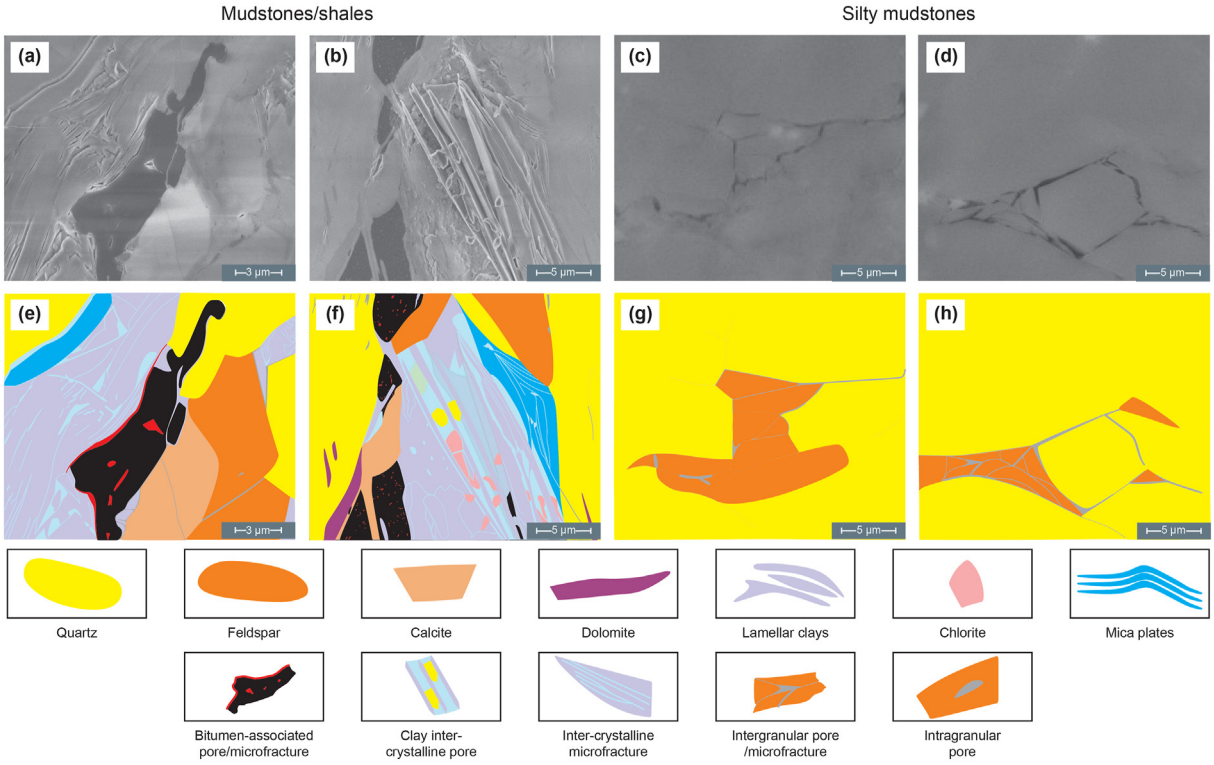

Fig. 15. Proposed conceptual model for elaborating a differential reservoir-forming mechanism and corresponding two-sided (positive and negative) effect on petrophysical and reservoir quality properties for the continental silty-mud sediments of the Upper Triassic Xujiahe Formation. (a, b) Classical phenomenon that appears bitumen-associated pores, clay inter-crystalline pores, and concomitant microfracture systems developed in the mudstone/shale reservoirs; (c, d) Classical phenomenon that appears residual intergranular pores and weakly developed microfractures developed in the silty mudstone reservoirs; (e, f) Schematic model illustrating a better reservoir performance-forming pattern of argillaceous sediments due to the development of bitumen-associated and clay inter-crystal pores; (g, h) Schematic model illustrating a relatively poorer reservoir quality in silty mudstone sediments due to the scarcity of bitumen particles and clay minerals.

from 10 to 100 nm, respectively, and significantly higher amounts for all specific intervals of argillaceous pore width distribution are statistically calculated, when compared with the results from investigation of silty mudstones (Fig. 14). This is in good agreement with the quantitative assessment criteria for defining microfractures in argillaceous reservoirs, demonstrating microcracks characterized by a great length-width ratio and a width less than 1 μm (He, 2015; Wang et al., 2015). Another substantial evidence come from quantitative extraction of plane porosity of the representative FE-SEM images, and all the selected mudstone/shale samples yield fundamentally higher values of Phi, Phi (P) and Phi (C), characterized by a wide gap between the argillaceous (Phi: 6.19%–15.56%, mean 9.31%; Phi (P): 2.51%–6.21%, mean 3.61%; Phi (C): 3.68%–9.35%, mean 5.70%) and silty facies (Phi: 1.22%–2.90%, mean 1.81%; Phi (P): 0.51%–1.21%, mean 0.76%; Phi (C): 0.71%–1.69%, mean 1.06%) (Fig. 14).

In turn, a conceptual model has been established to illustrate the reservoir-forming processes that act in continental silty-mud sediments of the Upper Triassic Xujiahe Formation (Fig. 15). This lends new valuable insight into a differential reservoir-forming mechanism and a corresponding two-sided (positive and negative) effect on petrophysical and reservoir quality properties for mudstone/shale and silty mudstone sedimentary units, respectively.

6. Conclusions

(1) Better reservoir properties are identified in mudstone/shale reservoirs as characterized by apparently higher micro-mesopore volumes and surface areas, and by better physical properties (especially average permeability) relative to those of silty mudstones, suggesting that argillaceous reservoirs are rich in storage spaces and permeable migration pathways/channels for natural gas.

(2) Widely distributed bitumen pores developed adjacent to brittle mineral particles or within clay-organic nanocomposites are supposed to be in favour of shrinking microcracks, which are conductive to formation of microbedding fractures, non-bedding microfractures, and even connected fracture/pore-fracture networks in mud-shale sediments. Furthermore, the marked enrichment of clay minerals in continental argillaceous reservoirs results in the development of two types of inter-crystalline pores occurring along oriented clay aggregates/platelets, also prompting microcrack formation and improvements in reservoir capacity and quality due to interconnections and associations with intergranular pores.

(3) Widespread bitumen-hosted pores and higher concentrations of clay minerals are identified as two major interrelated drivers of better storage and permeability conditions in continental argillaceous reservoirs relative to silty mudstones undergoing an equivalent diagenesis regime. This study thus establish a conceptual model serving as a meaningful interpretative framework to gain new insight into dual (positive and negative) effects of fluvio-lacustrine silty-mud fine-grained sediments on petrophysical and reservoir quality properties of the Upper Triassic Xujiahe Formation.

Acknowledgements

This work was supported by the Science Foundation for

Distinguished Young Scholars of China University of Petroleum, Beijing (No. 2462020QNXZ004), the National Natural Science and Technology Major Project (No. 2016ZX05034-001 and 2017ZX05035-002).

References

Aplin, A.C., Macquaker, J.H.S., 2011. Mudstone diversity: origin and implications for source, seal, and reservoir properties in petroleum systems. AAPG Bull. 95 (12), 2031–2059. https://doi.org/10.1306/03281110162.

Bian, C.S., Wang, H.J., Wang, Z.C., et al., 2009. Controlling factors for massive accumulation of natural gas in the Xujiahe Formation in central Sichuan Basin. Oil Gas Geol. 30 (5), 548–556 (in Chinese with English abstract).

Cao, J., Zhou, W., 2015. Characteristics and controlling factors of organic pores in continental shale gas reservoir of Chang 7^{th} of Yanchang Formation, Ordos Basin. Acta Geol. Sin. 89 (s), 1–2. https://doi.org/10.1111/1755-6724.12302_1.

Chalmers, G.R., Bustin, R.M., Power, I.M., 2012. Characterization of gas shale pore systems by porosimetry, pycnometry, surface area, and field emission scanning electron microscopy/transmission electron microscopy image analyses: examples from Barnett Woodford, Haynesville, Marcellus, and Doig units. AAPG Bull. 96 (6), 1099–1119. https://doi.org/10.1306/10171111052.

Chen, D.X., Liu, Y.C., Pang, X.Q., et al., 2016a. Reservoir characteristics and its control on gas-bearing properties of the 5^{th} member of the Triassic Xujiahe Formation continental shale in the Sichuan Basin of China. Earth Sci. Front. 23 (1), 174–184. https://doi.org/10.13745/j.esf.2016.01.016 (in Chinese with English abstract).

Chen, J., Xiao, X.M., 2014. Evolution of nanoporosity in organic-rich shales during thermal maturation. Fuel 129, 173–181. https://doi.org/10.1016/j.fuel.2014.03.058.

Chen, L., Jiang, Z.X., Liu, Q.X., et al., 2019. Mechanism of shale gas occurrence: insights from comparative study on pore structures of marine and lacustrine shales. Mar. Petrol. Geol. 104, 200–216. https://doi.org/10.1016/j.marpetgeo.2019.03.027.

Chen, S.B., Han, Y.F., Fu, C.Q., et al., 2016b. Micro and nano-size pores of clay minerals in shale reservoirs: implication for the accumulation of shale gas. Sediment. Geol. 342, 180–190. https://doi.org/10.1016/j.sedgeo.2016.06.022.

Chen, W.L., Zhou, W., Luo, P., et al., 2013. Analysis of the shale gas reservoir in the lower Silurian Longmaxi Formation , Changxin 1 well , Southeast Sichuan Basin. Acta Petrol. Sin. 29 (3), 1073–1086 (in Chinese with English abstract).

Clift, P.D., Olson, E.D., Lechnowskyj, A., et al., 2019. Grain-size variability within a mega-scale point-bar system, False River, Louisiana. Sedimentology 66 (2), 408–434. https://doi.org/10.1111/sed.12528.

Dai, J., Gong, D., Ni, Y., et al., 2014. Stable carbon isotopes of coal-derived gases sourced from the Mesozoic coal measures in China. Org. Geochem. 74, 123–142. https://doi.org/10.1016/j.orggeochem.2014.04.002.

Dai, J.X., Zou, C.N., Dong, D.Z., et al., 2016. Geochemical characteristics of marine and terrestrial shale gas in China. Mar. Petrol. Geol. 76, 444–463. https://doi.org/10.1016/j.marpetgeo.2016.04.027.

DeReuil, A.A., Birgenheier, L.P., 2019. Sediment dispersal and organic carbon preservation in a dynamic mudstone-dominated system, Juana Lopez Member, Mancos Shale. Sedimentology 66 (3), 1002–1041. https://doi.org/10.1111/sed.12532.

Dewhurst, D.N., Siggins, A.F., Sarout, J., Raven, M., Nordgard-Bolas, H.M., 2011. Geomechanical and ultrasonic characterization of a Norwegian Sea shale. Geophysics 76, WA101–WA111. https://doi.org/10.1190/1.3569599.

Ding, W.L., Zhu, D.W., Cai, J.J., Gong, M.L., Chen, F.Y., 2013. Analysis of the developmental characteristics and major regulating factors of fractures in marine - continental transitional shale-gas reservoirs: a case study of the Carboniferous - Permian strata in the southeastern Ordos Basin, central China. Mar. Petrol. Geol. 45, 121–133. https://doi.org/10.1016/j.marpetgeo.2013.04.022.

Dong, D.Z., Shi, Z.S., Sun, S.S., et al., 2018. Factors controlling microfractures in black shale: a case study of Ordovician Wufeng formation Silurian Longmaxi Formation in Shuanghe Profile, Changning area, Sichuan Basin, SW China. Petrol. Explor. Dev. 45 (5), 763–774 (in Chinese with English abstract).

Espitalie, J., Laporte, L.J., Madec, M., et al., 1977. Methode rapide de caracterisation des roches mères, de leur potential petrolier et de leur degré d'evolution. Rev l'Institut français Pétrole. 32, 32–42.

Fenster, M.S., Dolan, R., Smith, J.J., 2016. Grain-size distributions and coastal morphodynamics along the southern Maryland and Virginia barrier islands. Sedimentology 63 (4), 809–823. https://doi.org/10.1111/sed.12239.

Ferrill, D.A., McGinnis, R.N., Morris, A.P., et al., 2014. Control of mechanical stratigraphy on bed-restricted jointing and normal faulting: Eagle Ford Formation, south-central Texas. AAPG Bull. 98, 2477–2506. https://doi.org/10.1306/08191414053.

Fu, J., Wu, S.H., Luo, A.X., et al., 2013. Reservoir quality and its controlling factors of Chang 8 and Chang 6 members in Longdong area, Ordos Basin. Earth Sci. Front. 20 (2), 98–107 (in Chinese with English abstract).

Gao, F.L., Song, Y., Li, Z., et al., 2018. Quantitative characterization of pore connectivity using NMR and MIP: a case study of the Wangyinpu and Guanyintang shales in the Xiuwu basin, Southern China. Int. J. Coal Geol. 197, 53–65. https://doi.org/10.1016/j.coal.2018.07.007.

Gao, F.L., Song, Y., Liang, Z.K., et al., 2019. Development characteristics of organic pore in the continental shale and its genetic mechanism: a case study of Shahezi Formation shale in the Changling fault depression of Songliao Basin. Acta Petrol. Sin. 40 (9), 1030–1044. https://doi.org/10.7623/syxb201909002 (in Chinese with English abstract).

Gao, X.Y., Liu, L.F., Jiang, F.J., et al., 2016. Analysis of geological effects on methane adsorption capacity of continental shale: a case study of the Jurassic shale in the Tarim Basin, northwestern China. Geol. J. 51 (6), 936–948. https://doi.org/10.1002/gj.2706.

Ge, D.S., Liu, Y.M., Liu, X.Q., et al., 2018. Application of grain size analysis in tight sandstone reservoir and sedimentary environment evaluation. Special Oil Gas Reservoirs 25 (1), 41–72. https://doi.org/10.3969/j.issn.1006-6535 (in Chinese with English abstract).

Gregg, S.J., Sing, K.S.W., 1982. Adsorption, Surface Area and Porosity, second ed. Academic Press, pp. 1–50. https://doi.org/10.1524/zpch.1969.63.1_4.220.

Guan, Q.Z., Dong, D.Z., Wang, S.F., et al., 2016. Analyses on differences of microstructure between marine and lacustrine facies shale reservoirs. Nat. Gas Geosci. 27 (3), 524–531 (in Chinese with English abstract).

Guo, J.C., Zhou, H.Y., Zeng, J., et al., 2020. Advances in low-field nuclear magnetic resonance (NMR) technologies applied for characterization of pore space inside rocks: a critical review. Petrol. Sci. 17, 1281–1297. https://doi.org/10.1007/s12182-020-00488-0.

He, D.F., Li, D.S., Zhang, G.W., et al., 2011a. Formaiton and evolution of multi-cycle superposed Sichuan Basin, China. China J. Geol. 46 (3), 589–606 (in Chinese with English abstract).

He, J.H., Ding, W.L., Jiang, Z.X., et al., 2016. Logging identification and characteristic analysis of the lacustrine organic-rich shale lithofacies: a case study from the Es_3^L shale in the Jiyang Depression, Bohai Bay Basin, Eastern China. J. Petrol. Sci. Eng. 145, 238–255. https://doi.org/10.1016/j.petrol.2016.05.017.

He, L., 2015. Petrophisical Evaluation the Microfracture-Typed Complex Carboniferous Carbonate Reservoirs in the Eastern Magrin of the Caspian Sea Basin (Doctoral Dissertation). Yangtze University, p. 156 (in Chinese with English Abstract).

He, Z.J., Liu, B.J., Wang, P., 2011b. Genesis of bedding fracture and its influences on reservoirs in Jurassic, Yongjin area, Junggar basin. Petrol. Geol. Recov .Effic. 18 (1), 15–17. https://doi.org/10.1016/S1003-9953(10)60145-4 (in Chinese with English abstract).

He, Z.L., Nie, H.K., Zhao, J.H., et al., 2017. Types and origin of nanoscale pores and fractures in Wufeng and Longmaxi shale in Sichuan Basin and its periphery. J. Nanosci. Nanotechnol. 17, 6626–6633. https://doi.org/10.1166/jnn.2017.14425.

Huang, J.L., Dong, D.Z., Li, J.Z., et al., 2016. Reservoir characteristics and its influence on continental shale: an example from Triassic Xujiahe Formation shale, Sichuan Basin. Earth Sci. Front. 23 (2), 158–166. https://doi.org/10.13745/j.esf.2016.02.016 (in Chinese with English abstract).

Huang, J.L., Zou, C.N., Dong, D.Z., et al., 2015. Geochemical and reservoir characteristics of the upper Triassic continental shale in the Sichuan Basin, China. Energy Explor. Exploit. 33 (3), 375–396. https://doi.org/10.1260/0144-5987.33.3.375.

Jiang, F.J., Hu, T., Liu, L.F., et al., 2018. Geochemical and geological characteristics of the Jurassic continental black shale in the southwestern depression of Tarim basin. Geol. J. 54 (3), 1115–1131. https://doi.org/10.1002/gj.3212.

Jiang, Z.X., Duan, H.J., Liang, C., et al., 2017. Classification of hydrocarbon-bearing fine-grained sedimentary rocks. J. Earth Sci. 28 (6), 963–976. https://doi.org/10.1007/s12583-016-0920-0.

Jin, L., 2010. Characteristics of Natural Gas Accumulation in Xujiahe Formation in the Middle of West Sichuan Depression. Master Thesis. Chengdu University of Technology (in Chinese with English abstract).

Jin, Y.X., Cai, X., Yuan, Y., Wu, Y., 2015. Clay mineral characteristics and geological significance in Silurian Longmaxi formation shale, southeastern Chongqing. Coal Geol. China 27 (2), 21–35. https://doi.org/10.3969/j.issn.1674-1803 (in Chinese with English abstract).

Jin, Z.J., Nie, H.K., Liu, Q.Y., et al., 2018. Source and seal coupling mechanism for shale gas enrichment in upper Ordovician Wufeng formation - lower Silurian Longmaxi Formation in Sichuan Basin and its periphery. Mar. Petrol. Geol. 97, 78–93. https://doi.org/10.1016/j.marpetgeo.2018.06.009.

Jin, Z.K., Shi, L., Yan, W., et al., 2016. Contribution sedimentary and diagenetic factors to clastic reservoir quality: quantitative determination by single factor comparison method. J. Palaeogeogr. 18 (4), 535–544. https://doi.org/10.7605/gdlxb.2016.04.039 (in Chinese with English abstract).

Kennedy, M.J., Löhr, S.C., Fraser, S.A., Baruch, E.T., 2014. Direct evidence for organic carbon preservation as clay-organic nanocomposities in a Devonian black shale; from deposition to diagenesis. Earth Planet Sci. Lett. 388, 59–70. https://doi.org/10.1016/j.epsl.2013.11.044.

Lai, J., Wang, G.W., Ran, Y., Zhou, Z.L., 2015. Predictive distribution of high-quality reservoirs of tight gas sandstones by linking diagenesis to depositional facies: evidence from Xu-2 sandstones in the Penglai area of the central Sichuan basin, China. J. Nat. Gas Sci. Eng. 23, 97–111. https://doi.org/10.1016/j.epsl.2013.11.044.

Lai, J., Wang, G.W., Wang, Z.Y., et al., 2018. A review on pore structure characterization in tight sandstones. Earth Sci. Rev. 177, 436–457. https://doi.org/10.1016/j.earscirev.2017.12.003.

Liang, C., Jiang, Z., Zhang, C., et al., 2014. The shale characteristics and shale gas exploration prospects of the Lower Silurian Longmaxi shale, Sichuan Basin, South China. J. Nat. Gas Sci. Eng. 21, 636–648. https://doi.org/10.1016/j.jngse.2014.09.034.

Li, J.Z., Zhen, M., Chen, X.M., et al., 2016. Connotation analyses, source-reservoir assemblage types and development potential of unconventional hydrocarbon in China. Petrol. Res. 1 (2), 135–148. https://doi.org/10.7623/syxb201505001.

Li, J.Z., Zheng, M., Chen, X.M., et al., 2015. Connotation analyses, source-reservoir

assemblage types and development potential of unconventional hydrocarbon in China. Acta Petrol. Sin. 36 (5), 521–532. https://doi.org/10.7623/syxb201505001 (in Chinese with English Abstract).
Li, T.W., Jiang, Z.X., Li, Z., et al., 2017. Continental shale pore structure characteristics and their controlling factors: a case study from the lower third member of the Shahejie Formation, Zhanhua Sag, Eastern China. J. Nat. Gas Sci. Eng. 45, 670–692. https://doi.org/10.1016/j.jngse.2017.06.005.
Liu, B., Shi, J.X., Fu, X.F., et al., 2018. Petrological characteristics and shale oil enrichment of lacustrine fine-grained sedimentary system: a case study of organic-rich shale in first member of Cretaceous Qingshankou Formation in Gulong Sag, Songliao Basin, NE China. Petrol. Explor. Dev. 45 (5), 828–838. https://doi.org/10.1016/S1876-3804(18)30091-0 (in Chinese with English abstract).
Liu, D., 2019. Comprehensive Evaluation of Tight Oil Sweet Spots in the Yanchang Formation from the Western Ordos Basin. Master Thesis. China University of Petroleum - Beijing (in Chinese with English abstract).
Liu, B., Shieber, J., Mastalerz, M., Teng, J., 2019a. Organic matter content and type variation in the sequence stratigraphic context of the Upper Devonian New Albany Shale, Illinois Basin. Sediment. Geol. 383, 101–120. https://doi.org/10.1016/j.sedgeo.2019.02.004.
Liu, D.D., Li, Z., Jiang, Z.X., et al., 2019b. Impact of laminae on pore structures of lacustrine shales in the southern Songliao Basin, NE China. J. Asian Earth Sci. 182, 103935. https://doi.org/10.1016/j.jseaes.2019.103935.
Liu, H., Zhang, S., Song, G., et al., 2017. A discussion on the origin of shale reservoir inter-laminar fractures in the Shahejie Formation of Paleogene, Dongying depression. J. Earth Sci. 28 (6), 1064–1077. https://doi.org/10.1007/s12583-016-0946-3.
Liu, Y.F., Hu, W.X., Cao, J., et al., 2019c. Fluid-rock interaction and its effects on the Upper Triassic tight sandstones in the Sichuan Basin, China: insights from petrographic and geochemical study of carbonate cements. Sediment. Geol. 383, 121–135. https://doi.org/10.1016/j.sedgeo.2019.01.012.
Li, X., Xu, M., Cai, J.G., et al., 2019. Structure characteristics and evolution characteristics of pores in mud shale in Dongying Sag. Petrol. Geol. Recov .Effic. 26 (1), 88–100 (in Chinese with English abstract).
Li, Y.H., Song, Y., Jiang, Z.X., et al., 2018. Major factors controlling lamina induced fractures in the Upper Triassic Yanchang formation tight oil reservoir, Ordos basin, China. J. Asian Earth Sci. 166, 107–119. https://doi.org/10.1016/j.jseaes.2018.07.040.
Li, Y.J., Shao, L.Y., Eriksson, K.A., et al., 2014. Linked sequence stratigraphy and tectonics in the Sichuan continental foreland basin, Upper Triassic Xujiahe Formation, southwest China. J. Asian Earth Sci. 88, 116–136. https://doi.org/10.1016/j.jseaes.2014.02.025.
Liu, Y., Zhang, J.C., Zhang, P., et al., 2018. Origin and enrichment factors of natural gas from the Lower Silurian Songkan Formation in northern Guizhou province. South China. Int. J. Coal Geol. 187, 20–29. https://doi.org/10.1016/j.coal.2018.01.004.
Li, Z.Y., Schieber, J., 2020. Application of sequence stratigraphic concepts to the upper Cretaceous Tunuk shale member of the Mancos shale formation, south-central Utah: Parasequence styles in shelfal mudstone strata. Sedimentology 67 (1), 118–151. https://doi.org/10.1111/sed.12637.
Loucks, R.G., Reed, R.M., Ruppel, S.C., Jarvie, D.M., 2009. Morphology, genesis, and distribution of nanometer-scale pores in siliceous mudstones of the Mississippian Barnett Shale. J. Sediment. Res. 79 (12), 848–861. https://doi.org/10.2110/jsr.2009.092.
Lu, H.Y., An, Z.S., 1997. Experimental study on the influence of different pretreatment procedures on the particle-size measurement of loess sediments. Chin. Sci. Bull. 42, 2535–2538.
Luis, M.Y., Augusto, N.V., César, V., et al., 2020. Reservoir architecture and heterogeneity distribution in floodplain sandstones: key features in outcrop, core and wireline logs. Sedimentology 67 (7), 3355–3388. https://doi.org/10.1111/sed.12747.
Luo, J.L., Liu, X.S., Fu, X.Y., et al., 2014. Impact of petrologic components and their diagenetic evolution on tight sandstone reservoir quality and gas yield: a case study from He 8 gas-bearing reservoir of Upper Paleozoic in northern Ordos Basin, 5. In: Editorial Committee of Earth Science-Journal of China University of Geosciences, 39, pp. 537–545 (in Chinese with English abstract).
Luo, S.R., Zhang, L.K., Lei, Y.H., et al., 2016. Structural heterogeneity of reservoir and its implication on hydrocarbon accumulation in deep zones. China Petrol. Explor. 21 (1), 28–36. https://doi.org/10.3969/j.issn.1672-7703.2016.01.003 (in Chinese with English abstract).
Lyu, W.Y., Zeng, L.B., Zhang, B.J., et al., 2017. Influence of natural fractures on gas accumulation in the Upper Triassic tight gas sandstones in the northwestern Sichuan Basin, China. Mar. Petrol. Geol. 83, 60–72. https://doi.org/10.1016/j.marpetgeo.2017.03.004.
Mastalerz, M., Schimmelmann, A., Drobniak, A., Chen, Y.Y., 2013. Porosity of Devonian and Mississippian New Albany Shale across a maturation gradient: insights from organic petrology, gas adsorption, and mercury intrusion. AAPG Bull. 97 (10), 1621–1643. https://doi.org/10.1306/04011312194.
Mendhe, V.A., Mishra, S., Varma, A.K., et al., 2017. Gas reservoir characteristics of the lower Gondwana shales in Raniganj Basin of eastern India. J. Petrol. Sci. Eng. 149, 649–664. https://doi.org/10.1016/j.petrol.2016.11.008.
Milliken, K., 2014. A compositional classification for grain assemblages in fine-grained sediments and sedimentary rocks. J. Sediment. Res. 84, 1185–1199. https://doi.org/10.2110/jsr.2014.92.
Milliken, K.L., Rudnicki, M., Awwiller, D.N., Zhang, T., 2013. Organic matter-hosted pore system, marcellus formation (devonian), Pennsylvania. AAPG Bull. 97 (2), 177–200. https://doi.org/10.1306/07231212048.
Milroy, P., Wright, V.P., Simms, M.J., 2019. Dryland continental mudstones: Deciphering environmental changes in problematic mudstones from the upper Triassic (Carnian to Norian) Mercia mudstone group, south-west Britain. Sedimentology 66 (7), 2557–2589. https://doi.org/10.1111/sed.12626.
Nole, M., Daigle, H., Milliken, K.L., Prodanovic, M., 2016. A method for estimating microporosity of fine-grained sediments and sedimentary rocks via scanning electron microscope image analysis. Sedimentology 63 (6), 1507–1521. https://doi.org/10.1111/sed.12271.
Olivarius, M., Weibel, R., Hjuler, M.L., et al., 2015. Diagenetic effects on porosity–permeability relationships in red beds of the lower Triassic Bunter sandstone Formation in the north German basin. Sediment. Geol. 321, 139–153. https://doi.org/10.1016/j.sedgeo.2015.03.003.
Ougier-Simonin, A., Renard, F., Boehm, C., Vidal-Gilbert, S., 2016. Microfracturing and microporosity in shales. Earth Sci. Rev. 162, 198–226. https://doi.org/10.1016/j.earscirev.2016.09.006.
Qian, M.H., Jiang, Q.G., Li, M.W., et al., 2017. Quantitative characterization of extractable organic matter in lacustrine shale with different occurrences. Petrol. Explor. Dev. 39 (2), 278–286 (in Chinese with English Abstract).
Rahman, H.M., Kennedy, M., Löhr, S., Dewhurst, D.N., 2017. Clay-organic association as a control on hydrocarbon generation in shale. Org. Geochem. 105, 42–55. https://doi.org/10.1016/j.orggeochem.2017.01.011.
Rouquerol, J., Avnir, D., Fairbridge, C.W., et al., 1994. Recommendations for the characterization of porous solids. Pure Appl. Chem. 66, 1739–1758. https://doi.org/10.1351/pac199466081739.
Scherdel, C., Reichenauer, G., Wiener, M., 2010. Relationship between pore volumes and surface areas derived from the evaluation of N_2-sorption data by DR-, BET and t-plot. Microporous Mesoporous Mater. 13, 572–575. https://doi.org/10.1016/j.micromeso.2010.03.034.
Schieber, J., Miclăuș, C., Seserman, A., et al., 2019. When a mudstone was actually a "sand": results of a sedimentological investigation of the bituminous marl formation (Oligocene), Eastern Carpathians of Romania. Sediment. Geol. 384, 12–28. https://doi.org/10.1016/j.sedgeo.2019.02.009.
Schulten, H., Leinweber, P., Theng, B.K.G., 1996. Characterization of organic matter in an interlayer clay-organic complex from soil by pyrolysis methylation-mass spectrometry. Geoderma 69, 105–118. https://doi.org/10.1016/0016-7061(95)00054-2.
Slatt, R.M., O'Brien, N.R., 2011. Pore types in the Barnett and Woodford gas shales: contribution to understanding gas storage and migration pathways in fine-grained rocks. AAPG Bull. 98 (12), 2017–2030. https://doi.org/10.1306/03301110145.
Sneider, R.M., Tinker, C.N., Meckel, L.D., 1978. Delta environment reservoir types and their characteristics. J. Petrol. Technol. 30 (11), 1539–1546.
Spears, D.A., Lundegard, P.D., Samuels, N.D., 1980. Field classification of fine-grained sedimentary rocks: discussion and reply. J. Sediment. Res. 51, 1031–1033.
Sun, M.D., Zhang, L.H., Hu, Q.H., et al., 2019. Pore connectivity and water accessibility in Upper Permian transitional shales, southern China. Mar. Petrol. Geol. 107, 407–422. https://doi.org/10.1016/j.marpetgeo.2019.05.035.
Sun, Y.S., Guo, S.B., 2016. Qualitative and quantitative characterization of shale microscopic pore characteristics based on image analysis technology. Adv. Earth Sci. 31 (7), 751–763. https://doi.org/10.11867/j.issn.1001-8166.2016.07.0751 (in Chinese with English abstract).
Su, S.Y., Jiang, Z.X., Shan, X.L., et al., 2018. The effects of shale pore structure and mineral components on shale oil accumulation in the Zhanhua Sag, Jiyang Depression, Bohai Bay Basin, China. J. Petrol. Sci. Eng. 165, 365–374. https://doi.org/10.1016/j.petrol.2018.02.030.
Tian, H., Pan, L., Xiao, X., et al., 2013. A preliminary study on the pore characterization of Lower Silurian black shales in the Chuandong thrust fold belt, southwestern China using low pressure N_2 adsorption and FE-SEM methods. Mar. Petrol. Geol. 48, 8–19. https://doi.org/10.1016/j.marpetgeo.2013.07.008.
Tissot, B.P., Welte, D.H., 1984. Petroleum Formation and Occurrence. Springer-Verlag, New York. https://doi.org/10.1007/978-3-642-87813-8.
Wan, L., Wang, Q.B., Zhao, G.X., et al., 2018. Quantitative characterization and main controlling factors of micro pore structure in different size sandstone of fan delta reservoirs: a case study of Ed_3 in Shijiutuo Uplift steep slope zone. Geol. Sci. Technol. Inf. 37 (5), 90–99 (in Chinese with English abstract).
Wang, C., Zhang, B.Q., Hu, Q.H., et al., 2019. Laminae characteristics and influence on shale gas reservoir quality of lower Silurian Longmaxi Formation in the Jiaoshiba area of the Sichuan Basin, China. Mar. Petrol. Geol. 109, 839–851. https://doi.org/10.1016/j.marpetgeo.2019.06.022.
Wang, F.T., Guo, S.B., 2019. Influential factors and model of shale pore evolution: a case study of a continental shale from the Ordos Basin. Mar. Petrol. Geol. 102, 271–282. https://doi.org/10.1016/j.marpetgeo.2018.12.045.
Wang, H.J., Bian, C.S., Shi, Z.S., 2011. The control of effective source-reservoir combination on the formation of gas reservoir of Xujiahe Formation, Sichuan Basin. Nat. Gas Geosci. 22 (1), 38–46 (in Chinese with English abstract).
Wang, J., Bao, C., Guo, Z., 1989. Formation and development of the Sichuan basin. In: Zhu, X. (Ed.), Chinese Sedimentary Basins: Amsterdam. Elsevier, pp. 147–163.
Wang, J.L., Zhu, Y.M., Guan, Y.P., Fang, H.H., 2015. Influential factors and forecast of microcrack development degree of Longmaxi Formation shales in Nanchuan Region, Chongqiong. Nat. Gas Geosci. 26 (8), 1579–1586 (in Chinese with English Abstract).
Wang, W., 2007. Quantitative Research of Factors Affecting Clastic Reservoir Properties. Master Thesis. China University of Petroleum (East China) (in Chinese

with English abstract).
Wang, X.H., Ding, W.L., Cui, L., et al., 2018. The developmental characteristics of natural fractures and their significance for reservoirs in the Cambrian Niutitang marine shale of the Sangzhi block, southern China. J. Petrol. Sci. Eng. 165, 831–841. https://doi.org/10.1016/j.petrol.2018.02.042.
Wang, X., Brian, K., Jin, M., et al., 2016. Central Asian aridification during the late Eocene to early Miocene inferred from preliminary study of shallow marine-eolian sedimentary rocks from northeastern Tajik Basin. Sci. China Earth Sci. 59 (6), 1242–1457. https://doi.org/10.1007/s11430-016-5282-z.
Wang, Y., Jin, C., Wang, L.H., et al., 2015. Characterization of pore structures of Jiulaodong formation shale in the Sichuan Basin by SEM with Ar-ion milling. Rock Miner. Anal. 34 (3), 278–285. https://doi.org/10.15898/j.cnki.11-2131/td.2015.03.003 (in Chinese with English abstract).
Weber, K.J., 1986. How heterogeneity affects oil recovery. In: Lake, L.W., Carroll Jr., H.B. (Eds.), Reservoir Characterization. Academic Press, New York, pp. 487–544. https://doi.org/10.1016/B978-0-12-434065-7.50021-6.
Wei, H.H., Liu, J.L., Meng, Q.R., 2010. Structural and sedimentary evolution of the southern Songliao Basin, northeast China, and implications for hydrocarbon prospectivity. AAPG Bull. 94 (4), 531–564. https://doi.org/10.1306/09080909060.
Worden, R.H., Mayall, M.J., Evans, I.J., 1997. Predicting reservoir quality during exploration: lithic grains, porosity and permeability in Tertiary clastic rocks of the South China Sea Basin. Geol. Soc. London Spec. 126 (1), 107–115. https://doi.org/10.1144/GSL.SP.1997.126.01.08.
Wu, L., Zong, W., Du, X.F., Li, P., 2019. Grain size analysis of sand-conglomerate of Paomagang Formation in Enshi Cretaceous basin, western Hubei Province. Resour. Environ. Eng. 33 (2), 164–169. https://doi.org/10.16536/j.cnki.Issn.1671-1211.2019.02.004 (in Chinese with English abstract).
Xu, C.M., Gehenn, J.-M., Zhao, D.H., et al., 2015. The fluvial and lacustrine sedimentary systems and stratigraphic correlation in the Upper Triassic Xujiahe Formation in Sichuan Basin, China. AAPG Bull. 99 (11), 2023–2041. https://doi.org/10.1306/07061514236.
Xue, B., Zhang, J.C., Tang, X., et al., 2015. Characteristics of microscopic pore and gas accumulation on shale in Longmaxi Formation, northwest Guizhou. Acta Petrol. Sin. 36 (2), 138–149. https://doi.org/10.7623/syxb201502002 (in Chinese with English abstract).
Xu, M., 2014. Research on the Diagenesis Evolution of Argillaceous Source Rock and its Nanometer Pore Structure. Master Thesis. Tongji University (in Chinese with English abstract).
Xu, M., Cai, J.G., Hao, Y.Q., et al., 2013. The study of nano-scale pore structure characteristics and controlling factors of shale reservoirs. In: The 14th National Meeting on Organic Geochemistry in China. Zhuhai, pp. 663–664 (in Chinese).
Xu, Z.Y., Zhang, X.Y., Wu, S.H., Zhao, Y., 2008. Genesis of the low-permeability reservoir bed of upper Triassic Xujiahe Formation in Xinchang gas field, western Sichuan depression. Petrol. Sci. 5 (3), 230–237. https://doi.org/10.1007/s12182-008-0035-z.
Yang, R.C., Jin, Z.J., van Loon AJT, et al., 2019a. Climatic and tectonic controls of lacustrine hyperpycnite origination in the Late Triassic Ordos Basin, central China: implications for unconventional petroleum development: Reply. AAPG Bull. 103 (2), 511–514. https://doi.org/10.1306/06101615095.
Yang, W., Zuo, R.S., Jiang, Z.X., et al., 2018. Effect of lithofacies on pore structure and new insights into pore-preserving mechanisms of the over-mature Qiongzhusi marine shales in Lower Cambrian of the southern Sichuan Basin, China. Mar. Petrol. Geol. 98, 746–762. https://doi.org/10.1016/j.marpetgeo.2018.09.020.
Yang, W., Zuo, R.S., Chen, D.X., et al., 2019b. Climate and tectonic-driven deposition of sandwiched continental shale units: new insights from petrology, geochemistry, and integrated provenance analyses (the western Sichuan subsiding Basin, Southwest China). Int. J. Coal Geol. 211, 103227. https://doi.org/10.1016/j.coal.2019.103227.
Yang, Y.L., Aplin, A.C., 1998. Influence of lithology and effective stress on the pore size distribution and modelled permeability of some mudstones from the Norwegian margin. Mar. Petrol. Geol. 15, 163–175. https://doi.org/10.1016/S0264-8172(98)00008-7.
Yang, Y.L., Aplin, A.C., 2007. Permeability and petrophysical properties of 30 natural mudstones. J. Geophys. Res. 112, B03206. https://doi.org/10.1029/2005JB004243.
Yang, Z., Zou, C.N., Wu, S.T., et al., 2019c. Formation, distribution and resource potential of the "sweet areas (sections)" of continental shale oil in China. Mar. Petrol. Geol. 102, 48–60. https://doi.org/10.1016/j.marpetgeo.2018.11.049.
Yao, J.L., Deng, X.Q., Zhao, Y.D., et al., 2013. Characteristics of tight oil in Triassic Yanchang Formation, Ordos Basin. Petrol. Explor. Dev. 40 (2), 161–169. https://doi.org/10.1016/S1876-3804(13)60019-1.
Yawar, Z., Schieber, J., 2017. On the origin of silt laminae in laminated shales. Sediment. Geol. 360, 22–34. https://doi.org/10.1016/j.sedgeo.2017.09.001.
Yin, P., 2003. Study on Sedimentary Facies and Diagnosis of Chang-2 Oil-Bearing Beds of the Upper Triassic Yanchang Formation in Yanchang Region. Ph.D. Thesis. Northwest University (in Chinese with English abstract).
Yu, X.H., Wang, J.Z., Liang, J.Q., et al., 2014. Depositional characteristics and accumulation model of gas hydrates in northern South China Sea. Mar. Petrol. Geol. 56, 74–86. https://doi.org/10.1016/j.marpetgeo.2014.03.011.
Zeng, X.M., Zhang, H., Zou, M.S., et al., 2016. Provenance analysis and influence on reservoir physical property of the 3rd member of Liushagang Formation in eastern Wushi depression, Beibu Gulf basin. Geol. Sci. Technol. Inf. 35 (6), 63–69 (in Chinese with English abstract).
Zhang, B., Zhang, J.J., Yan, S.Y., et al., 2012. Detrital quartz and quartz cement in Upper Triassic reservoir sandstones of the Sichuan basin: characteristics and mechanisms of formation based on cathodoluminescence and electron backscatter diffraction analysis. Sediment. Geol. 267–268, 104–114. https://doi.org/10.1016/j.sedgeo.2012.05.015.
Zhang, C., Zhu, D.Y., Luo, Q., et al., 2017. Major factors controlling fracture development in the Middle Permian Lucaogou Formation tight oil reservoir, Junggar Basin, NW China. J. Asian Earth Sci. 146, 279–295. https://doi.org/10.1016/j.jseaes.2017.04.032.
Zhang, X.J., 2005. Analysis on the major controlling factors of reservoir properties of the extra-low porosity and extra-low permeability sandstones of the Fuxian targeted area, Ordos Basin. In: The 1st National Special Oil & Gas Reservoirs Technology Symposium in China. Beijing, pp. 27–31 (in Chinese).
Zhang, Y.Y., He, Z.L., Jiang, S., et al., 2019. Fracture types in the lower Cambrian shale and their effect on shale gas accumulation, Upper Yangtze. Mar. Petrol. Geol. 99, 282–291. https://doi.org/10.1016/j.marpetgeo.2018.10.030.
Zhao, W.Z., Wang, H.J., Xu, C.C., et al., 2010. Reservoir-forming mechanism and enrichment conditions of the extensive Xujiahe Formation gas reservoirs, central Sichuan Basin. Petrol. Explor. Dev. 37 (2), 146–157. https://doi.org/10.1016/s1876-3804(10)60022-5.
Zheng, H.B., Powell, C.M., Butcher, K., Cao, J.J., 2003. Late Neogene loess deposition in southern Tarim Basin: tectonic and palaeoenvironmental implcations. Tectonophysics 375, 49–59. https://doi.org/10.1016/S0040-1951(03)00333-0.
Zhou, L.H., Pu, X.G., Deng, Y., et al., 2016. Several issues in studies on fine-grained sedimentary rocks. Lit. Res. 28 (1), 6–15. https://doi.org/10.3969/j.issn.1673-8926.2016.01.002 (in Chinese with English Abstract).
Zhu, G.Y., Wang, T.S., Xie, Z.Y., et al., 2015. Giant gas discovery in the Precambrian deeply buried reservoirs in the Sichuan basin, China: implications for gas exploration in old cratonic basins. Precambrian Res. 262, 45–66. https://doi.org/10.1016/j.precamres.2015.02.023.
Zhu, R.K., Zhao, X., Liu, L.H., et al., 2009. Depositional system and favorable reservoir distribution of Xujiahe Formation in Sichuan Basin. Petrol. Explor. Dev. 36 (1), 46–55. https://doi.org/10.1016/s1876-3804(09)60110-5.
Zhu, X.M., Zheng, J.M., Gu, J.Y., et al., 2008. Sedimentary Petrology. Petroleum Industry Press, Beijing.
Zou, C.N., Dong, D.Z., Wang, S.J., et al., 2010. Geological characteristics and resource potential of shale gas in China. Petrol. Explor. Dev. 37 (6), 641–653. https://doi.org/10.1016/S1876-3804(11)60001-3.
Zou, C.N., Yang, Z., Zhang, G.S., et al., 2014. Conventional and unconventional petroleum "orderly accumulation": concept and practical significance. Petrol. Explor. Dev. 44, 14–27. https://doi.org/10.1016/S1876-3804(14)60002-1.
Zou, C.N., Zhu, R.K., Chen, Z.Q., et al., 2019. Organic-matter-rich shales of China. Earth Sci. Rev. 189, 51–78. https://doi.org/10.1016/j.earscirev.2018.12.002.